Characterization of Pro-Fibrotic Signaling Pathways using Human Hepatic Organoids

Yuan Guan, Zhuoqing Fang, Angelina Hu, Sarah Roberts, Meiyue Wang, Wenlong Ren, Patrik K. Johansson[1], Sarah C.Heilshorn[1], Annika Enejder[1] and Gary Peltz[*]

Department of Anesthesia, Pain and Perioperative Medicine, Stanford University School of Medicine, Stanford CA, 94305; and [1]Department of Materials Science and Engineering, Stanford University, Stanford CA, 94305

Figures: 5

Key Words: Liver Fibrosis, Hepatic Organoids, Pharmacology

Author Contributions. Y.G, S.R., A.H., P.K.J generated experimental data; Z.F., Y.G., P.K.J., A.E., M.W., W.R., S.C.H. and G.P. analyzed data; The paper was written by Y.G. and G.P with input from all authors.

Word Count: 5703 (including references)

Financial support: Y.G. and G.P. were supported by awards from the NIDDK (1R56DK12930901A1). P.K.J., S.C.H., and A.E were supported by awards from the National Science Foundation (CBET 2033302).

The authors have declared that no conflict of interest exists.

*Address Correspondence to: gpeltz@stanford.edu 300 Pasteur Dr. Room L232 Stanford, CA 94305.

Abstract

Background: Due to the limitations of available *in vitro* systems and animal models, we lack a detailed understanding of the pathogenetic mechanisms and have minimal treatment options for liver fibrosis.
Methods: To overcome this barrier, we engineered a live cell imaging system that identifies collagen producing cells in a human multi-lineage hepatic organoid. This system was adapted for use as a microwell-based platform (i.e., microHOs) where exposure to PDGF or TGFβ1 induced the formation of thick collagen fibers.
Results: Transcriptomic analysis revealed that TGFβ1 exposure converted a sub-population of hepatic stellate-like cells into myofibroblast-like cells, which contribute to the development of liver fibrosis. When pro-fibrotic intracellular signaling pathways were examined using pharmacological probes, the anti-fibrotic effect of receptor-specific tyrosine kinase inhibitors was limited to the fibrosis induced by the corresponding growth factor, which indicates that their anti-fibrotic efficacy would be limited to fibrotic diseases that were solely mediated by that growth factor. In contrast, GSK3β or p38 MAPK inhibitors could prevent TGFβ1- or PDGF-induced fibrosis in microHOs because they block intracellular signaling pathways that are commonly utilized by the TGFβ1 and PDGF receptors.
Conclusions: these studies identified GSK3β and p38 MAPK inhibitors as potential new broad-spectrum therapies for liver fibrosis, and it is likely that other new therapies could subsequently be identified using this microHO system.

Word count: 213

Abbreviations: ARPKD, Autosomal Recessive Polycystic Kidney Disease; ECM, extra-cellular matrix; GSEA, gene set enrichment analysis; HCS, high content screening; HO, hepatic organoid; HCC, hepatocellular carcinoma; HSC, hepatic stellate cells; iPSC, induced pluripotent stem cells; MAPK, Mitogen Activated Protein Kinase; NASH, non-alcoholic steatohepatitis; SHG, Second Harmonic Generation.

Liver fibrosis is a pathological condition caused by the accumulation of extracellular matrix (**ECM**) that develops in response to chronic liver injury [1, 2]. It results from an interaction between parenchymal and nonparenchymal liver cells and involves endogenous and liver infiltrating immune cells [3-5]. The key non-parenchymal cell is the myofibroblast, which is generated when a fibrogenic stimulus induced by liver injury causes hepatic stellate cells (**HSC**) to transdifferentiate into myofibroblasts that produce fibril-forming collagens and other ECM components [5-9]. Before organoid methodology was available, *in vitro* models often did not have the spectrum of cell types that mediate fibrogenesis, which limited our ability to explore fibrogenic mechanisms. Commonly used rodent models require an injury inducing agent (carbon tetrachloride, bile duct ligation, or dietary modulation); are very time consuming and expensive to run; and any conclusions drawn from them are limited by concerns about their fidelity with the processes mediating the commonly occurring forms of human liver fibrosis [10]. However, the pathogenesis of liver fibrosis can best be studied using a multi-lineage human hepatic organoid (**HO**) that has the cellular components and the geometry of hepatic lobules, which enables the effect that biochemical signals have on fibrosis to be quantitatively characterized. We previously developed an *in vitro* model system that differentiates human induced pluripotent stem cells (**iPSCs**) into a multi-lineage HO that has hepatocytes, cholangiocytes, HSCs, and cells of other lineages (fibroblasts, macrophages, and endothelial cells); and bile ducts and other structures found in the liver lobule are formed in these HOs [11, 12]. HOs engineered to express a causative mutation for Autosomal Recessive Polycystic Kidney Disease (**ARPKD**) developed an extensive fibrosis [12] that was characterized by a marked increase in thick collagen fiber formation, which resembled that in liver tissue obtained from ARPKD patients. The myofibroblasts in ARPKD organoids resembled those in the livers of patients with viral-induced cirrhosis or advanced non-alcoholic steatohepatitis (**NASH**) [12]. Here, we engineered a live cell imaging system for identification of the collagen producing cells in hepatic organoids that was adapted for use in a microwell-based platform. This system was used to characterize the signals driving liver fibrosis at the whole organoid, single cell, and molecular levels. Moreover, when the interaction between the intracellular signaling pathways activated by two pro-fibrotic factors were characterized using pharmacological agents, two potential new approaches for treating liver fibrosis were identified.

Results

A live cell imaging system for hepatic fibrosis. Collagen is a triple helical protein that is composed of two COL1A1 (α1) and one COL1A2 (α2) chains, and increased collagen synthesis

by activated myofibroblasts is a major contributor to liver fibrosis [2]. To characterize fibrogenic mechanisms, we developed a live cell imaging system, which enabled collagen producing cells in HOs to be identified and quantitatively analyzed. A CRISPR-assisted insertion tagging system (CRISPaint) [13] was used to insert a Clover expression cassette (***COL1A1*-P2A Clover**) at the COOH terminus of the endogenous *COL1A1* gene in a control iPSC line. Since the insert has a self-cleaving P2A peptide, *COL1A1* mRNA expressing cells in the HOs produced from *COL1A1*-P2A Clover iPSCs were labelled with a fluorescent intracellular protein (**Fig 1A-B**). The Clover$^+$ cell population increased in HO cultures at the hepatoblast stage (day 9) (**Fig. 1C-D**). Immunostaining and flow cytometry revealed that Clover$^+$ cells: were markedly increased in day 21 HOs that were treated with TGFβ1 or PDGFβ (on day 13); co-expressed PDGFRβ and COL1A1; were present throughout the organoid; and were distinct from hepatocytes or cholangiocytes (**Figs. 1E-G, S1; Tables S1-S2**). Flow cytometry results confirm that Clover fluorescence is cell based (Figs. 1D, 1G). The pro-fibrotic effect of TGFβ and PDGF was consistent with the temporal pattern of expression of the mRNAs encoding their receptors (*PDGFRA, PDGFRB, TGFBR1, TGFBR2, TGFBR3, BMPR1B*) and intracellular signaling proteins (STATs, SMADs), which were expressed at the hepatoblast stage (day 9) (i.e., prior to when microHOs are exposed to PDGF or TFGβ on day 13) and in mature HOs (**Fig. S2**). Clover protein was not expressed in iPSC or hepatoblasts, but was expressed in control, TGFβ- and PDGF-treated HOs (**Fig. 1H**).

The spatial distribution and morphology of the collagen fibers in HOs were examined using Second Harmonic Generation (**SHG**) microscopy [14, 15], which has previously been used to quantitatively analyze liver fibrosis in human patients [16, 17] and to monitor fibrosis in ARPKD HOs [12]. Of importance, SHG measures thick collagen fiber formation; which is a complex biochemical pathway that requires the coordinated activity of multiple liver enzymes that include proteases and other post-translational processing enzymes that act on collagen, and subsequently the activity of lysyl hydroxylases and lysyl oxidases to generate thick collagen fibers. [18]. SHG images revealed that control HOs had sporadic networks of cross-linked collagen fibers surrounding the cells in some isolated regions, while the TGFβ1 or PDGF-treated organoids had more extensive networks of thick collagen fibers throughout the entire HO. A quantitative comparison indicated that TGFβ1 ($p < 0.05$) or PDGF ($p < 0.01$) exposure induced statistically significant increases in total collagen abundance and in the abundance of thick collagen fibers (i.e., > 3 um diameter) formed in HOs ($p<0.01$) (**Fig. 1I**). The SHG and immunostaining results

indicate that PDGF or TGFβ1 increases the numbers of collagen synthesizing cells and the amount of thick collagen fibers formed in HOs.

*A high content screening system (**HCS**) for serially monitoring the effect of biochemical signals on liver fibrosis*. Culture conditions were modified to enable HOs to reproducibly grow to a standard size in microwells, which we refer to as '*microHOs*' (**Fig. 2A-B**). (**Fig. 2A-B**). Trichrome staining confirmed that TGFβ or PDGF induced a large increase in collagen in microHOs (**Fig. 2C**). The TGFβ effect on thick collagen fiber formation was confirmed by 4-hydroxyproline (4OH-Pro) measurements: 4OH-Pro was absent in iPSC; it increased in day 9 hepatoblasts and in day 21 control HOs; but was significantly increased after PDGF or TGFβ exposure ($p<0.001$ vs control) (**Fig. 2D**). HCS was performed using a confocal fluorescence microplate imager with an automated program that we developed for analyzing multiple Z-stacked confocal images. TGFβ1 addition on day 13 induced a sustained increase in $COL1A1^+$ cells in microHOs that was blocked by co-administration of TGFRβ1 tyrosine kinase inhibitors (10 uM SB431542 [19, 20] or A83-01 [21]) (**Fig. 2E-F**). PDGFβ addition on day 13 also increased the number of $COL1A1^+$ cells in microHOs, which was blocked by addition of a PDGFRβ tyrosine kinase inhibitor (10 uM Imatinib [22, 23]) (**Fig. 3, top**). The microHO system was also used to examine the effect of five cytokines (IL-4 [24], IL-6 [25], IL-13, IL-33 [26, 27], TNFα [28]) and three growth factors (IGF1 [29], VEGF [30], CCL3 [31]) that had been directly or indirectly implicated in the pathogenesis of NASH or liver fibrosis. None of these agents induced fibrosis in microHOs (**Fig. S3**). Analysis of the temporal pattern of receptor expression in differentiating HO cultures using previously obtained transcriptomic data [12] revealed that the mRNAs encoding the IGF-1 (*IGF1R*), IL13 (*IL13RA1*), and VEGF (*VEGFR-1* (*FLT1*); *VEGFR-2 (KDR*)) receptors were expressed in day 9 hepatoblasts and in mature (day 21) organoids. In contrast, the mRNAs encoding the receptors for IL33 (*IL1RL1 or ST2*), IL4 (*IL4R*), or for the common gamma chain that is used for intra-cellular signaling by multiple cytokine receptors (*IL2RG*) were not expressed in day 9 hepatoblasts (**Fig. S4A**). Of note, the mRNAs encoding most of these receptors are abundantly expressed in mature HOs (**Fig. S4B**). Hence, the lack of a profibrotic effect of IGF-1 and VEGF is not due to the absence of receptor expression on day 9, which is prior to when microHOs were exposed to these agents. However, the lack of a profibrotic effect of IL-4 and IL-13 could result from the absence of functional receptors on day 9, which is just before the time of exposure to those cytokines.

Since hedgehog signaling pathway activation increases *COL1A1* mRNA expression in myofibroblasts [32, 33] and promotes myofibroblast accumulation and liver fibrosis [34], we examined whether a hedgehog pathway activator would induce fibrosis in microHOs. Smoothened (**SMO**) is a seven transmembrane protein [35, 36] that accumulates in the primary cilium, and transduces a Hedgehog pathway signal intracellularly. However, addition of a SMO agonist (SAG), which activates Hedgehog signaling [37], did not induce fibrosis in microHO cultures (Fig. S3).

We next examined whether addition of seven free fatty acids (at 0 to 400 uM concentrations), which included their saturated and corresponding cis-9 (or trans-9) monounsaturated forms, on day 13 to microHO cultures had a pro-fibrotic effect. Previously obtained transcriptomic data from developing and mature HO cultures revealed that the mRNAs encoding proteins required for free fatty acid uptake (i.e., *SLC27A1, SCC27A5, FABP5, and Acyl-CoA Binding protein* (*ACBP*)) are expressed in day 9 HO cultures (**Fig. S5**). Even when the free fatty acids were added at concentrations below those previously reported to induce fibrosis in other types of HOs [38], the cells within microHOs abundantly accumulated fatty acids from the medium and there was evidence of lipotoxicity (**Fig. S6**). Somewhat unexpectedly based upon the results presented in [38], free fatty acid addition did not have a pro-fibrotic effect in microHOs (**Fig. S7**). The disparate findings may result from their using organoid stiffness [38] (rather than an increase in collagen thick fibers) as the criteria for fibrosis. Our results, which are consistent with recent findings by others [39], indicate that free fatty acid addition causes steatosis and lipotoxicity, but does not cause the fibrosis that develops in the advanced clinical stages of NASH. Altered differentiation conditions, adding other factors, or co-culture with other cell types may be required to enable HOs to model NASH-associated fibrosis.

Transcriptomic analysis. To molecularly characterize the pro-fibrotic effects of PDGFβ and TGFβ1, scRNA-Seq data was generated from day 21 control (22,211 cells), TGFβ1-treated (17,554 cells) or PDGFβ-treated (18,013 cells) microHOs. Eleven cell clusters were identified by analysis of the combined scRNA-Seq data (**Fig. 4A-B, Table S3**) and the cells in the PDGF- or TGFβ1-treated microHOs were reproducibly different from those in control microHOs (**Fig. S8A-C**). The differentially expressed genes in each cluster were analyzed to identify the cell type of each cluster (**Tables S4-S5**). Based upon expression of canonical mRNAs and by the level of concordance between the cell cluster transcriptomes and the cell types in human liver, the microHOs have cholangiocyte (Cho1-3), hepatocyte (Hep), mesenchymal cell (Mes1-4) and

myofibroblast (MyoF_T1-2, MyoF_P) clusters. One myofibroblast cluster (MyoF_T1) was far more abundant in TGFβ1-treated microHOs than in control or PDGF-treated microHOs (37.5% of total vs <2%), while another myofibroblast cluster (MyoF_P) was more abundant in PDGF-treated microHOs than in control or TGFβ1-treated microHOs (20% of total vs <2%). The abundance of a mesenchymal cluster (Mes2) was markedly decreased in TGFβ or PDGF-treated microHOs (25% vs <5%) (Table S3). A one-way ANOVA comparing the different types of cells in each of 5-independent biological replicates analyzed by scRNA-Seq indicated that MyoF_T1 ($p<0.015$) and MyoF_P ($p<0.05$) abundances were significantly increased, while Mes2 abundance was decreased ($p=0.004$) in TGFβ- or PDGF-treated microHOs (**Table S6**). Transcriptomic comparisons with various cell types in control and cirrhotic human liver were performed to further characterize the three clusters whose abundance was significantly altered by TGFβ or PDGF exposure. The results revealed that MyoF_T1 and MyoF_P clusters were most like that of myofibroblasts, whereas Mes2 was most similar to HSC in human liver (**Fig. 4C, Fig. S9, Tables S7-S8)**. As described in supplemental note 1, Gene Set Enrichment Analysis (**GSEA**) [40] revealed that the gene expression signature of MyoF_T1 in microHOs resembled those found in fibrotic human liver tissue caused by NASH or hepatocellular carcinoma (**Fig. 4D**, **Fig. S10**, **Table S9**). While the MyoF_P gene signature was positively associated with NASH or HCC-induced liver fibrotic tissue, those GSEA associations did not achieve statistical significance. Also, *COL1A1* and *Clover* mRNAs have an identical pattern of expression in the microHOs: both mRNAs are expressed in myofibroblasts and mesenchymal cells. In contrast, *EPCAM* mRNA (a hepatoblast and cholangiocyte marker) was not expressed in the *Clover* mRNA$^+$ cells (**Fig. 4E-F).** The mRNAs found in cholangiocytes (*KRT19*, *KRT7* and *CFTR)* or in hepatocytes and cholangiocytes (*HNF4A, AFP, CDH1, ALDHA1, APOB, FGB*) were not expressed in the *Clover* mRNA$^+$ cells in the microHOs (**Fig. S11**). Myofibroblast marker mRNA (*ACTA2, PDGFRA, FAP*) expression was very low in control microHOs, but they were predominantly expressed in the myofibroblast (MyoF_T1/2, MyoF_P) clusters in PDGF- or TGFβ-treated microHOs (**Fig. S12**). Consistent with the profile of *FAP* mRNA expression in microHOs (Fig. S10), FAP is absent in most tissues under basal conditions but is highly expressed on activated myofibroblasts [41, 42]. FAP is a well-established marker for activated fibroblasts [43] and its serine protease activity promotes liver fibrosis by activating HSC and promoting macrophage infiltration after liver injury [44]. The pattern of expression of 9 mesenchyme and myofibroblast-specific mRNAs in mesenchymal cells and myofibroblasts in human liver is retained in Mes2 and MyoF_T1 cells in microHOs (**Fig. S13**). Taken together, the

transcriptomic results indicate that TGFβ1 or PDGF exposure converts a population of HSC-like cells into myofibroblast-like cells in microHOs.

Pharmacologic characterization of pro-fibrotic signaling pathways. PDGF and TGFβ1 are well established drivers of liver fibrosis [45]. TGFRB activation leads to activation of SMAD signaling pathways [46, 47] and PDGFR cross-linking activates the STAT3 pathway [48] [49], and both of these pathways have well-known roles in promoting hepatic fibrosis [49]. Since PDGFRβ and TGFβR1 inhibitors could block the PDGFβ and TGFβ1-induced increase in COL1A1$^+$ cells, respectively; the interaction between these intracellular signaling pathways was examined in microHOs. The TGFRβ inhibitor did not block the PDGFβ-induced increase, and the PDGFRβ inhibitor did not block the TGFβ1-induced increase in COL1A1$^+$ cells (Fig. 3). Also, addition of the combination of PDGFβ and TGFβ1 did not significantly increase the number of COL1A1$^+$ cells in microHOs relative to that caused by either factor alone (Fig. 3, bottom).

Although the anti-fibrotic effect of the receptor tyrosine kinase inhibitors was growth factor dependent, other signaling pathways that are jointly activated by the TGFβ1 and PDGF receptors could be essential for fibrosis. Both TGFRB [46, 47, 50] and PDGFR [51, 52] activate the p38 Mitogen Activated Protein Kinase (MAPK) and PI3K–Akt–mTOR intracellular signaling pathways, which are also pro-fibrotic. Therefore, we examined whether co-administration of PI3K-Akt-mTOR (rapamycin) or MAPK pathway (SB202190) inhibitors with PDGF or TGFβ1 on day 13 could reduce fibrosis. Co-administration of 10 uM SB202190 – an ATP pocket binding and highly selective p38α and β kinase inhibitor [53] – inhibited both TGFβ1 and PDGF-induced fibrosis in microHOs (**Fig. 5A-C**). Thus, p38 MAPK pathway activity is essential for either PDGF- or TGFβ1-driven fibrosis. Rapamycin partially inhibited PDGF-induced fibrosis but did not inhibit TGFβ1-induced fibrosis (**Fig. 5D-F**). The lack of inhibition of TGFβ1-induced fibrosis by rapamycin indicated that the downstream part of the PI3K-Akt-mTOR pathway was not essential for TGFβ1-induced fibrosis, but it may be required for PDGF-induced fibrosis.

WNT/β-catenin signaling contributes to the pathogenesis of liver fibrosis and NASH [54, 55], which led to the suggestion that it could be targeted by anti-fibrotic therapies [56]. Since glycogen synthase kinase 3β (GSK3β)-mediated phosphorylation of β-catenin targets it for ubiquitin-dependent proteasomal degradation, GSK3β inhibitors will stabilize β-catenin and promote the transcription of β-catenin target mRNAs [57, 58]. Therefore, we examined the effect

that co-administration of a Wnt/β-catenin pathway activator (Wnt3a) or of a GSK3β enzyme inhibitor (10 uM CHIR99021), which has been shown to activate the Wnt/β-catenin pathway [59], had on fibrosis in microHOs. Wnt3a co-administration had a minimal effect on the extent of PDGF- or TGFβ1-driven fibrosis (Fig. S3). The GSK3β inhibitor by itself did not increase COL1A1$^+$ cells in the organoids (Fig. S3). However, co-administration of the GSK3β inhibitor with either PDGF or TGFβ1 blocked fibrosis in microHOs (Fig. 3). Of importance, cell viability in microHOs was not reduced by addition of TGFβ1, nor by adding the GSK3β or TGFRβ inhibitors **(Fig. S14).** Our results indicate that p38 MAPK or GSK3β kinase inhibitors can block liver fibrosis irrespective of whether it is driven by either PDGF or TGFβ1.

This microHO system could also be used to test the potential anti-fibrotic efficacy of candidate medications for liver fibrosis. For example, nintedanib and pirfenidone are the only two FDA-approved drugs for treatment of pulmonary fibrosis [60]. Both inhibit multiple tyrosine kinases and have been shown to reduce lung fibrosis in animal models [61-63] and in patients with interstitial lung fibrosis [64-68]. Although the mechanism for their anti-fibrotic effect is unknown, it has been suggested that they could also be used to treat liver fibrosis [49]. However, co-administration of 10 uM pirfenidone or 10 uM nintedanib did not inhibit the TGFβ1-induced fibrosis in microHOs. While pirfenidone did not inhibit PDGF-induced fibrosis, nintedanib delayed the onset of PDGF-induced fibrosis in microHOs (**Fig. 5D-F**). Of note, these concentrations were >10-fold above the nintedanib concentration that inhibited PDGF-stimulated cellular proliferation (IC_{50} 64 nM) and PDGFR auto-phosphorylation (IC_{50} 22-39 nM) [69] and of the pirfenidone concentration (1 uM) that inhibited proliferation and TGFβ mRNA expression [70] in cultured human fibroblasts. The partial inhibitory effect of nintedanib of PDGF-induced fibrosis is consistent with its inhibition of the PDGF receptor tyrosine kinase activity (IC_{50} 60 nM) [71].

To determine if the anti-fibrotic effects of the TGFRβ, GSK3β or p38 inhibitors was dependent upon the genetic background of the *COL1A1*-P2A Clover line, we examined their anti-fibrotic effect in microHOs generated from iPSC lines (C1, C2) prepared from two other donors with different genetic backgrounds [11]. As visualized by trichrome staining, TGFβ induced a marked increase in collagen-rich connective tissue in the C1 and C2 microHOs ($p<0.001$), which was markedly inhibited by addition of TGFRβ, GSK3β, or p38 inhibitors ($p<0.001$) (**Fig. 6**). These results indicate that their anti-fibrotic effect was independent of genetic background.

Discussion

We demonstrate that microHOs and the live cell imaging system developed here can be used to characterize the biochemical signals and intracellular signaling pathways that drive liver fibrosis and for assessing potential anti-fibrotic therapies. The TGFβ1 and PDGF-induced fibrosis in microHOs was shown to resemble human fibrotic liver disease based upon the formation of thick collagen fibers (SHG results), increased collagen crosslinking (4-OHPro measurement) and increased collagen deposition (trichrome staining) in microHOs; and by transcriptomic comparisons demonstrating that the transcriptomes of microHO myofibroblasts resembled the myofibroblasts in fibrotic human liver tissue. Of the twenty agents tested using microHOs – which included cytokines, growth factors, fatty acids, a hedgehog agonist, and Wnt ligands – only PDGF and TGFβ1 had a strong pro-fibrotic effect. For several of the cytokines, growth factors and fatty acids tested, the absence of a pro-fibrotic effect in the organoid could be due to the absence of an immune system and/or of other cell types that could be required for a pro-fibrotic effect. However, a key finding emerging from this study is that the anti-fibrotic efficacy of PDGFR and TGFRβ tyrosine kinase inhibitors was dependent upon the factor driving the fibrosis, and this could explain why it has been so difficult to develop therapies for liver fibrosis. When fibrosis is driven by PDGFRβ-STAT3 pathway activation – as occurs in ARPKD liver fibrosis [12] or in murine models of lung and bone marrow fibrosis [72] – PDGFR inhibitors will exhibit anti-fibrotic efficacy; but they will be less effective when the fibrosis is driven by other mechanisms. There are organ-specific and species-specific differences in the mechanisms mediating tissue fibrosis [10] and different types of liver injury produces different patterns of liver fibrosis in humans [73]. Consistent with differences in the factors that drive different types of fibrosis, microHO data indicates that at least one (and possibly both) of the FDA approved drugs for treatment of lung fibrosis drugs may not be effective for liver fibrosis. As another example, a combination treatment with PDGFR (imatinib) and TGFRβ (galunisertib [74]) inhibitors was more effective than blockade of either pathway alone in a murine radiation-induced lung fibrosis model [75]. To optimally treat liver fibrosis, therapies may have to be adjusted based upon the pathogenic driving factors, which may vary in different patients or in response to different inciting causes. There is already evidence that Diabetes patients can be subdivided into distinct sub-groups based upon clinical features and biomarker results [76], and efforts are underway to optimize treatment selection for the different types of diabetes patients [77]. Just as in other diseases, application of the principles of '*precision medicine'* (i.e., using genetic or genomic

information to optimize treatment selection [78]) could enable therapies for liver fibrosis to be successfully developed.

Another key finding was that GSK3β and p38 MAPK inhibitors potently blocked the fibrosis induced by TGFβ1 or PDGF. The GSK3β inhibitor effect was unexpected since modulating Wnt/β-catenin signaling has had variable effects on liver fibrosis in mouse models [79, 80]; and in a murine bile duct ligation model, GSK3β inhibitor administration produced an increase the extent of liver fibrosis [81]. As discussed in supplemental note 2, there are multiple nodes where the TGFβ, Wnt/β-catenin and the p38 MAPK pathways interact. These interactions could explain how a GSK3β inhibitor could block TGFβ-induced fibrosis; but the mechanism for the GSK3β inhibitor effect on PDGF-induced fibrosis is less clear. Nevertheless, our results indicate that the p38 MAPK pathway, which is activated by both TGFβ1 and PDGF receptors, plays a key role in fibrosis. Although there was no prior data demonstrating that it had an effect on liver fibrosis, the ability of SB202190 to inhibit fibrosis in microHOs is consistent with prior studies showing that this agent inhibited the development of renal interstitial [82] and corneal [83] fibrosis in animal models, and the conversion of human corneal fibroblasts into myofibroblasts *in vitro* [84]. However, additional studies will have to be performed to characterize the mechanism(s) by which the Wnt/β-catenin and p38 MAPK pathways, along with the SMAD and STAT3 pathways that are also activated by TGFβ1 and PDGF receptors, jointly contribute to liver fibrosis. Moreover, microHOs can also be used in conjunction with other recently developed genomic methods to provide a deeper understanding of the mechanisms mediating liver fibrosis [85]. In summary, live cell imaging of human microHOs has identified GSK3β and p38 MAPK inhibitors as potential new therapies for liver fibrosis, and it is likely that other new therapies and their mechanism of action could subsequently be identified using this system.

Data availability. All raw and processed single cell RNA-seq data were deposited in the Gene Expression Omnibus (GEO) and are available under accession GSE228214.

References

[1] Yoon YJ, Friedman SL, Lee YA. Antifibrotic Therapies: Where Are We Now? Semin Liver Dis 2016;36:87-98.
[2] Hernandez-Gea V, Friedman SL. Pathogenesis of liver fibrosis. Annual review of pathology 2011;6:425-456.

[3] Pinzani M, Luong TV. Pathogenesis of biliary fibrosis. Biochim Biophys Acta Mol Basis Dis 2018;1864:1279-1283.
[4] Pinzani M. Pathophysiology of Liver Fibrosis. Dig Dis 2015;33:492-497.
[5] Zhang CY, Yuan WG, He P, Lei JH, Wang CX. Liver fibrosis and hepatic stellate cells: Etiology, pathological hallmarks and therapeutic targets. World J Gastroenterol 2016;22:10512-10522.
[6] Tsuchida T, Friedman SL. Mechanisms of hepatic stellate cell activation. Nature reviews Gastroenterology & hepatology 2017;14:397-411.
[7] Yin C, Evason KJ, Asahina K, Stainier DY. Hepatic stellate cells in liver development, regeneration, and cancer. J Clin Invest 2013;123:1902-1910.
[8] Zhang DY, Goossens N, Guo J, Tsai MC, Chou HI, Altunkaynak C, et al. A hepatic stellate cell gene expression signature associated with outcomes in hepatitis C cirrhosis and hepatocellular carcinoma after curative resection. Gut 2016;65:1754-1764.
[9] Mederacke I, Hsu CC, Troeger JS, Huebener P, Mu X, Dapito DH, et al. Fate tracing reveals hepatic stellate cells as dominant contributors to liver fibrosis independent of its aetiology. Nature communications 2013;4:2823.
[10] Mehal WZ, Iredale J, Friedman SL. Scraping fibrosis: expressway to the core of fibrosis. Nat Med 2011;17:552-553.
[11] Guan Y, Xu D, Garfin PM, Ehmer U, Hurwitz M, Enns G, et al. Human Hepatic Organoids for the Analysis of Human Genetic Diseases. JCI Insight 2017;2:pii: 94954.
[12] Guan Y, Enejder A, Wang M, Fang Z, Cui L, Chen SY, et al. A human multi-lineage hepatic organoid model for liver fibrosis. Nature communications 2021;12:6138.
[13] Schmid-Burgk JL, Honing K, Ebert TS, Hornung V. CRISPaint allows modular base-specific gene tagging using a ligase-4-dependent mechanism. Nature communications 2016;7:12338.
[14] Campagnola PJ, Loew LM. Second-harmonic imaging microscopy for visualizing biomolecular arrays in cells, tissues and organisms. Nat Biotechnol 2003;21:1356-1360.
[15] Deniset-Besseau A, Duboisset J, Benichou E, Hache F, Brevet PF, Schanne-Klein MC. Measurement of the second-order hyperpolarizability of the collagen triple helix and determination of its physical origin. J Phys Chem B 2009;113:13437-13445.
[16] Sun W, Chang S, Tai DC, Tan N, Xiao G, Tang H, et al. Nonlinear optical microscopy: use of second harmonic generation and two-photon microscopy for automated quantitative liver fibrosis studies. J Biomed Opt 2008;13:064010.
[17] Gailhouste L, Le Grand Y, Odin C, Guyader D, Turlin B, Ezan F, et al. Fibrillar collagen scoring by second harmonic microscopy: a new tool in the assessment of liver fibrosis. J Hepatol 2010;52:398-406.
[18] Yamauchi M, Sricholpech M. Lysine post-translational modifications of collagen. Essays Biochem 2012;52:113-133.
[19] Laping NJ, Grygielko E, Mathur A, Butter S, Bomberger J, Tweed C, et al. Inhibition of transforming growth factor (TGF)-beta1-induced extracellular matrix with a novel inhibitor of the TGF-beta type I receptor kinase activity: SB-431542. Mol Pharmacol 2002;62:58-64.
[20] Inman GJ, Nicolas FJ, Callahan JF, Harling JD, Gaster LM, Reith AD, et al. SB-431542 is a potent and specific inhibitor of transforming growth factor-beta superfamily type I activin receptor-like kinase (ALK) receptors ALK4, ALK5, and ALK7. Mol Pharmacol 2002;62:65-74.

[21] Tojo M, Hamashima Y, Hanyu A, Kajimoto T, Saitoh M, Miyazono K, et al. The ALK-5 inhibitor A-83-01 inhibits Smad signaling and epithelial-to-mesenchymal transition by transforming growth factor-beta. Cancer Sci 2005;96:791-800.
[22] Puckett RL, Lorey F, Rinaldo P, Lipson MH, Matern D, Sowa ME, et al. Maple syrup urine disease: further evidence that newborn screening may fail to identify variant forms. Mol Genet Metab 2010;100:136-142.
[23] Breedveld P, Pluim D, Cipriani G, Wielinga P, van Tellingen O, Schinkel AH, et al. The Effect of Bcrp1 (Abcg2) on the In vivo Pharmacokinetics and Brain Penetration of Imatinib Mesylate (Gleevec): Implications for the Use of Breast Cancer Resistance Protein and P-Glycoprotein Inhibitors to Enable the Brain Penetration of Imatinib in Patients. Cancer Research 2005;65:2577-2582.
[24] Weng SY, Wang X, Vijayan S, Tang Y, Kim YO, Padberg K, et al. IL-4 Receptor Alpha Signaling through Macrophages Differentially Regulates Liver Fibrosis Progression and Reversal. EBioMedicine 2018;29:92-103.
[25] Paquissi FC. Immunity and Fibrogenesis: The Role of Th17/IL-17 Axis in HBV and HCV-induced Chronic Hepatitis and Progression to Cirrhosis. Front Immunol 2017;8:1195.
[26] Marvie P, Lisbonne M, L'Helgoualc'h A, Rauch M, Turlin B, Preisser L, et al. Interleukin-33 overexpression is associated with liver fibrosis in mice and humans. J Cell Mol Med 2010;14:1726-1739.
[27] Tan Z, Liu Q, Jiang R, Lv L, Shoto SS, Maillet I, et al. Interleukin-33 drives hepatic fibrosis through activation of hepatic stellate cells. Cell Mol Immunol 2018;15:388-398.
[28] Lu S, Wang Y, Liu J. Tumor necrosis factor-alpha signaling in nonalcoholic steatohepatitis and targeted therapies. J Genet Genomics 2022;49:269-278.
[29] Adamek A, Kasprzak A. Insulin-Like Growth Factor (IGF) System in Liver Diseases. International journal of molecular sciences 2018;19.
[30] Mariotti V, Fiorotto R, Cadamuro M, Fabris L, Strazzabosco M. New insights on the role of vascular endothelial growth factor in biliary pathophysiology. JHEP Rep 2021;3:100251.
[31] Xu L, Chen Y, Nagashimada M, Ni Y, Zhuge F, Chen G, et al. CC chemokine ligand 3 deficiency ameliorates diet-induced steatohepatitis by regulating liver macrophage recruitment and M1/M2 status in mice. Metabolism: clinical and experimental 2021;125:154914.
[32] Hu B, Phan SH. Myofibroblasts. Curr Opin Rheumatol 2013;25:71-77.
[33] Choi SS, Omenetti A, Syn WK, Diehl AM. The role of Hedgehog signaling in fibrogenic liver repair. Int J Biochem Cell Biol 2011;43:238-244.
[34] Syn WK, Jung Y, Omenetti A, Abdelmalek M, Guy CD, Yang L, et al. Hedgehog-mediated epithelial-to-mesenchymal transition and fibrogenic repair in nonalcoholic fatty liver disease. Gastroenterology 2009;137:1478-1488 e1478.
[35] Chen JK, Taipale J, Cooper MK, Beachy PA. Inhibition of Hedgehog signaling by direct binding of cyclopamine to Smoothened. Genes Dev 2002;16:2743-2748.
[36] Taipale J, Chen JK, Cooper MK, Wang B, Mann RK, Milenkovic L, et al. Effects of oncogenic mutations in Smoothened and Patched can be reversed by cyclopamine. Nature 2000;406:1005-1009.
[37] Chen JK, Taipale J, Young KE, Maiti T, Beachy PA. Small molecule modulation of Smoothened activity. Proc Natl Acad Sci U S A 2002;99:14071-14076.

[38] Ouchi R, Togo S, Kimura M, Shinozawa T, Koido M, Koike H, et al. Modeling Steatohepatitis in Humans with Pluripotent Stem Cell-Derived Organoids. Cell metabolism 2019;30:374-384.
[39] Hendriks D, Brouwers JF, Hamer K, Geurts MH, Luciana L, Massalini S, et al. Engineered human hepatocyte organoids enable CRISPR-based target discovery and drug screening for steatosis. Nat Biotechnol 2023; https://doi.org/10.1038/s41587-023-01680-4.
[40] Subramanian A, Tamayo P, Mootha VK, Mukherjee S, Ebert BL, Gillette MA, et al. Gene set enrichment analysis: a knowledge-based approach for interpreting genome-wide expression profiles. Proc Natl Acad Sci U S A 2005;102:15545-15550.
[41] Levy MT, McCaughan GW, Marinos G, Gorrell MD. Intrahepatic expression of the hepatic stellate cell marker fibroblast activation protein correlates with the degree of fibrosis in hepatitis C virus infection. Liver 2002;22:93-101.
[42] Gorrell MD, Wang XM, Levy MT, Kable E, Marinos G, Cox G, et al. Intrahepatic expression of collagen and fibroblast activation protein (FAP) in hepatitis C virus infection. Adv Exp Med Biol 2003;524:235-243.
[43] Lay AJ, Zhang HE, McCaughan GW, Gorrell MD. Fibroblast activation protein in liver fibrosis. Front Biosci (Landmark Ed) 2019;24:1-17.
[44] Yang AT, Kim YO, Yan XZ, Abe H, Aslam M, Park KS, et al. Fibroblast Activation Protein Activates Macrophages and Promotes Parenchymal Liver Inflammation and Fibrosis. Cell Mol Gastroenterol Hepatol 2022;15:841-867.
[45] Frangogiannis N. Transforming growth factor-beta in tissue fibrosis. J Exp Med 2020;217:e20190103.
[46] Zhang YE. Non-Smad Signaling Pathways of the TGF-beta Family. Cold Spring Harbor perspectives in biology 2017;9.
[47] Budi EH, Duan D, Derynck R. Transforming Growth Factor-beta Receptors and Smads: Regulatory Complexity and Functional Versatility. Trends Cell Biol 2017;27:658-672.
[48] Vignais ML, Gilman M. Distinct mechanisms of activation of Stat1 and Stat3 by platelet-derived growth factor receptor in a cell-free system. Mol Cell Biol 1999;19:3727-3735.
[49] Ying HZ, Chen Q, Zhang WY, Zhang HH, Ma Y, Zhang SZ, et al. PDGF signaling pathway in hepatic fibrosis pathogenesis and therapeutics (Review). Mol Med Rep 2017;16:7879-7889.
[50] Budi EH, Schaub JR, Decaris M, Turner S, Derynck R. TGF-beta as a driver of fibrosis: physiological roles and therapeutic opportunities. J Pathol 2021;254:358-373.
[51] Razmara M, Heldin CH, Lennartsson J. Platelet-derived growth factor-induced Akt phosphorylation requires mTOR/Rictor and phospholipase C-gamma1, whereas S6 phosphorylation depends on mTOR/Raptor and phospholipase D. Cell Commun Signal 2013;11:3.
[52] Pan S, Hu Y, Hu M, Jian H, Chen M, Gan L, et al. Platelet-derived PDGF promotes the invasion and metastasis of cholangiocarcinoma by upregulating MMP2/MMP9 expression and inducing EMT via the p38/MAPK signalling pathway. Am J Transl Res 2020;12:3577-3595.
[53] Frantz B, Klatt T, Pang M, Parsons J, Rolando A, Williams H, et al. The activation state of p38 mitogen-activated protein kinase determines the efficiency of ATP competition for pyridinylimidazole inhibitor binding. Biochemistry 1998;37:13846-13853.
[54] Annunziato S, Sun T, Tchorz JS. The RSPO-LGR4/5-ZNRF3/RNF43 module in liver homeostasis, regeneration, and disease. Hepatology 2022;76:888-899.

[55] Perugorria MJ, Olaizola P, Labiano I, Esparza-Baquer A, Marzioni M, Marin JJG, et al. Wnt-beta-catenin signalling in liver development, health and disease. Nature reviews Gastroenterology & hepatology 2019;16:121-136.
[56] Tian L, Wang Y, Jang YY. Wnt signaling in biliary development, proliferation, and fibrosis. Exp Biol Med (Maywood) 2022;247:360-367.
[57] MacDonald BT, Tamai K, He X. Wnt/beta-catenin signaling: components, mechanisms, and diseases. Dev Cell 2009;17:9-26.
[58] Nusse R, Clevers H. Wnt/beta-Catenin Signaling, Disease, and Emerging Therapeutic Modalities. Cell 2017;169:985-999.
[59] Sato N, Meijer L, Skaltsounis L, Greengard P, Brivanlou AH. Maintenance of pluripotency in human and mouse embryonic stem cells through activation of Wnt signaling by a pharmacological GSK-3-specific inhibitor. Nat Med 2004;10:55-63.
[60] Finnerty JP, Ponnuswamy A, Dutta P, Abdelaziz A, Kamil H. Efficacy of antifibrotic drugs, nintedanib and pirfenidone, in treatment of progressive pulmonary fibrosis in both idiopathic pulmonary fibrosis (IPF) and non-IPF: a systematic review and meta-analysis. BMC Pulm Med 2021;21:411.
[61] Wollin L, Wex E, Pautsch A, Schnapp G, Hostettler KE, Stowasser S, et al. Mode of action of nintedanib in the treatment of idiopathic pulmonary fibrosis. Eur Respir J 2015;45:1434-1445.
[62] Iyer SN, Gurujeyalakshmi G, Giri SN. Effects of pirfenidone on transforming growth factor-beta gene expression at the transcriptional level in bleomycin hamster model of lung fibrosis. J Pharmacol Exp Ther 1999;291:367-373.
[63] Wang Q, Wang Y, Hyde DM, Gotwals PJ, Koteliansky VE, Ryan ST, et al. Reduction of bleomycin induced lung fibrosis by transforming growth factor beta soluble receptor in hamsters. Thorax 1999;54:805-812.
[64] Richeldi L, du Bois RM, Raghu G, Azuma A, Brown KK, Costabel U, et al. Efficacy and safety of nintedanib in idiopathic pulmonary fibrosis. N Engl J Med 2014;370:2071-2082.
[65] Flaherty KR, Wells AU, Cottin V, Devaraj A, Walsh SLF, Inoue Y, et al. Nintedanib in Progressive Fibrosing Interstitial Lung Diseases. N Engl J Med 2019;381:1718-1727.
[66] Richeldi L, Costabel U, Selman M, Kim DS, Hansell DM, Nicholson AG, et al. Efficacy of a tyrosine kinase inhibitor in idiopathic pulmonary fibrosis. N Engl J Med 2011;365:1079-1087.
[67] Lancaster LH, de Andrade JA, Zibrak JD, Padilla ML, Albera C, Nathan SD, et al. Pirfenidone safety and adverse event management in idiopathic pulmonary fibrosis. Eur Respir Rev 2017;26.
[68] Costabel U, Albera C, Lancaster LH, Lin CY, Hormel P, Hulter HN, et al. An Open-Label Study of the Long-Term Safety of Pirfenidone in Patients with Idiopathic Pulmonary Fibrosis (RECAP). Respiration 2017;94:408-415.
[69] Wollin L, Maillet I, Quesniaux V, Holweg A, Ryffel B. Antifibrotic and anti-inflammatory activity of the tyrosine kinase inhibitor nintedanib in experimental models of lung fibrosis. J Pharmacol Exp Ther 2014;349:209-220.
[70] Lin X, Yu M, Wu K, Yuan H, Zhong H. Effects of pirfenidone on proliferation, migration, and collagen contraction of human Tenon's fibroblasts in vitro. Invest Ophthalmol Vis Sci 2009;50:3763-3770.

[71] Hilberg F, Roth GJ, Krssak M, Kautschitsch S, Sommergruber W, Tontsch-Grunt U, et al. BIBF 1120: triple angiokinase inhibitor with sustained receptor blockade and good antitumor efficacy. Cancer Res 2008;68:4774-4782.
[72] Decker M, Martinez-Morentin L, Wang G, Lee Y, Liu Q, Leslie J, et al. Leptin-receptor-expressing bone marrow stromal cells are myofibroblasts in primary myelofibrosis. Nat Cell Biol 2017;19:677-688.
[73] Friedman SL, Pinzani M. Hepatic fibrosis 2022: Unmet needs and a blueprint for the future. Hepatology 2022;75:473-488.
[74] Yingling JM, McMillen WT, Yan L, Huang H, Sawyer JS, Graff J, et al. Preclinical assessment of galunisertib (LY2157299 monohydrate), a first-in-class transforming growth factor-beta receptor type I inhibitor. Oncotarget 2018;9:6659-6677.
[75] Dadrich M, Nicolay NH, Flechsig P, Bickelhaupt S, Hoeltgen L, Roeder F, et al. Combined inhibition of TGFbeta and PDGF signaling attenuates radiation-induced pulmonary fibrosis. Oncoimmunology 2016;5:e1123366.
[76] Ahlqvist E, Storm P, Karajamaki A, Martinell M, Dorkhan M, Carlsson A, et al. Novel subgroups of adult-onset diabetes and their association with outcomes: a data-driven cluster analysis of six variables. Lancet Diabetes Endocrinol 2018;6:361-369.
[77] Perreault L, Skyler JS, Rosenstock J. Novel therapies with precision mechanisms for type 2 diabetes mellitus. Nat Rev Endocrinol 2021;17:364-377.
[78] Zeggini E, Gloyn AL, Barton AC, Wain LV. Translational genomics and precision medicine: Moving from the lab to the clinic. Science 2019;365:1409-1413.
[79] Zhuang S, Hua X, He K, Zhou T, Zhang J, Wu H, et al. Inhibition of GSK-3beta induces AP-1-mediated osteopontin expression to promote cholestatic liver fibrosis. FASEB J 2018;32:4494-4503.
[80] Pradhan-Sundd T, Kosar K, Saggi H, Zhang R, Vats R, Cornuet P, et al. Wnt/beta-Catenin Signaling Plays a Protective Role in the Mdr2 Knockout Murine Model of Cholestatic Liver Disease. Hepatology 2020;71:1732-1749.
[81] Thompson MD, Moghe A, Cornuet P, Marino R, Tian J, Wang P, et al. beta-Catenin regulation of farnesoid X receptor signaling and bile acid metabolism during murine cholestasis. Hepatology 2018;67:955-971.
[82] Prakash J, Sandovici M, Saluja V, Lacombe M, Schaapveld RQ, de Borst MH, et al. Intracellular delivery of the p38 mitogen-activated protein kinase inhibitor SB202190 [4-(4-fluorophenyl)-2-(4-hydroxyphenyl)-5-(4-pyridyl)1H-imidazole] in renal tubular cells: a novel strategy to treat renal fibrosis. J Pharmacol Exp Ther 2006;319:8-19.
[83] Nassar K, Tura A, Luke J, Luke M, Grisanti S, Grisanti S. A p38 MAPK inhibitor improves outcome after glaucoma filtration surgery. J Glaucoma 2015;24:165-178.
[84] Guo X, Sriram S, Tran JA, Hutcheon AEK, Zieske JD. Inhibition of Human Corneal Myofibroblast Formation. Invest Ophthalmol Vis Sci 2018;59:3511-3520.
[85] Guan Y, Peltz G. Hepatic Organoids Move from Adolescence to Maturity. Liver International 2024;DOI: 10.1111/liv.15893.
[86] Ramachandran P, Dobie R, Wilson-Kanamori JR, Dora EF, Henderson BEP, Luu NT, et al. Resolving the fibrotic niche of human liver cirrhosis at single-cell level. Nature 2019;575:512-518.

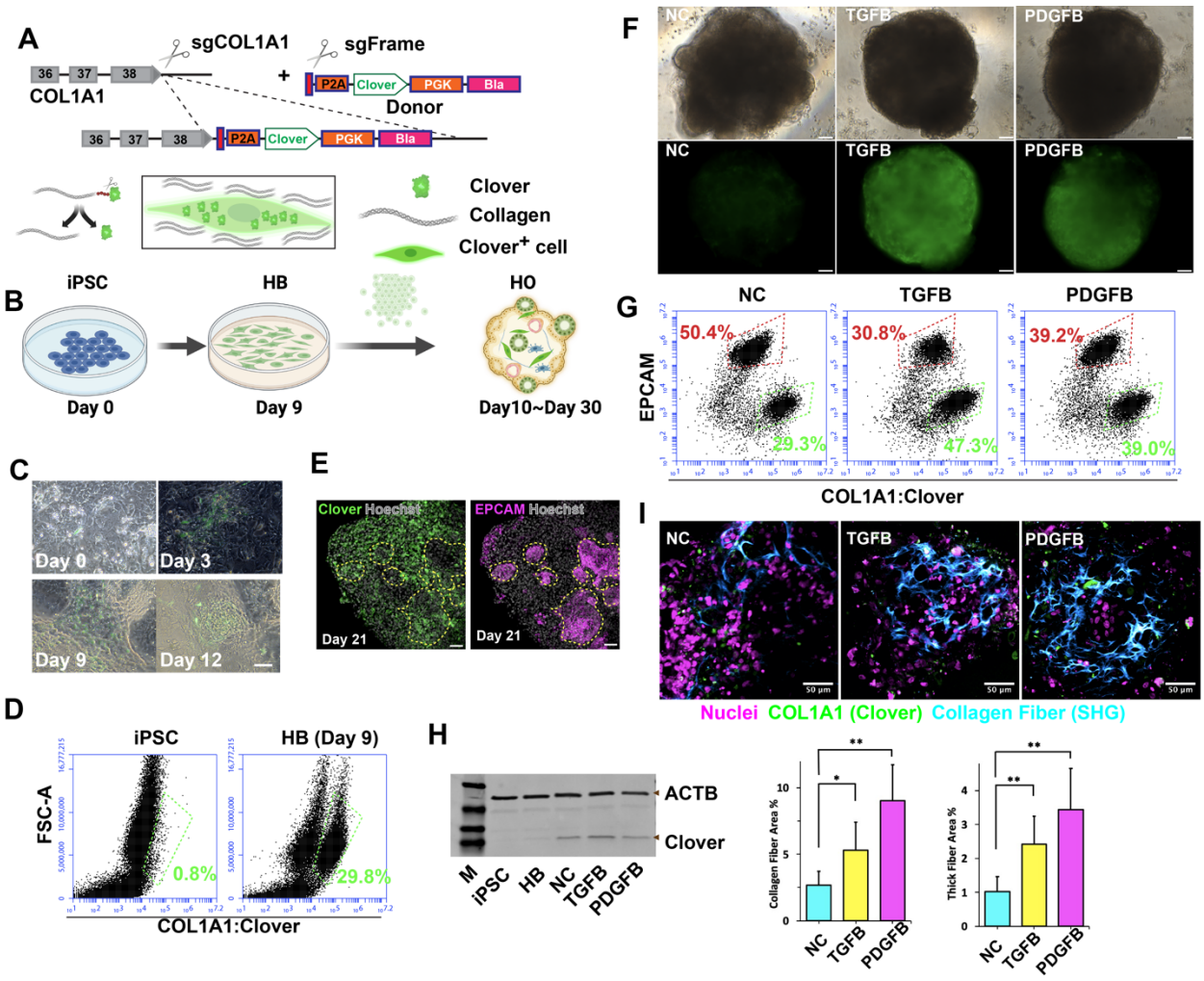

Figure 1. (A) *Top:* A diagram of the CRISPaint system used to insert P2A-Clover at the 3' end of *COL1A1* in an iPSC line. After blasticidin selection, cells were cloned to generate the COL1A1-P2A-Clover iPSC line. *Bottom*: The self-cleaving P2A peptide enables *COL1A1* expressing cells to be labelled with a fluorescent intracellular protein (Clover). (**B**) The collagen producing cells in a HO produced from COL1A1-P2A-Clover iPSCs are labelled with an intracellular fluorescent Clover protein. (**C**) An overlay of bright field and fluorescent images of differentiating COL1A1-P2A Clover HO cultures reveals that the number of Clover$^+$ cells increase between days 3 and 12. Scale bar: 50 μm. (**D**) Flow cytometry scatter plots show that the Clover$^+$ cell population is absent in iPSC (day 0) but appears in (day 9) hepatoblasts in differentiating *COL1A1*-P2A Clover HO cultures. (**E**) Stacked confocal images show the location of antibody-stained EPCAM$^+$ (bottom) or fluorescent Clover$^+$ (top) cells in day 20 COL1A1-P2A-Clover organoids. The yellow dashed circles (bottom) indicate areas with EPCAM$^+$ (i.e., hepatocytes or cholangiocytes) cells; and Clover$^+$ cells are not found

within those areas but are present in other areas of the HO. Scale bar: 50 μm. (**F**) Bright field (top) and fluorescence (bottom) images of day 21 *COL1A1*-P2A Clover HOs treated on day 13 with no addition (NC), 50 ng/ml TGFβ1 or 50 ng/ml PDGFβ. Both growth factors induced a marked increase in COL1A1$^+$ cells. Scale bars, 50 μm. (**G**) Flow cytometry scatter plots show that Clover$^+$ cells are increased in mature day 21 *COL1A1*-P2A Clover HOs after TGFβ or PDGF exposure. Also, the Clover$^+$ cells are distinct from the EPCAM$^+$ (hepatocytes or cholangiocytes) cells in the HOs. (**H**) Immunoblot showing Clover protein expression in differentiating HO cultures (iPSC, day 9 hepatoblasts (HB)); and in day 21 control (NC), PDGF- or TGFβ-treated HOs. The positions of Clover and β-actin (ACTB) proteins are indicated. (**I**) SHG analysis of the collagen fibers formed in human HOs. *Top:* Depth color-coded projections of collagen fibers within day 21 control organoids, or day 21 organoids that were treated with 50 ng/ml TGFβ1 or 50 ng/ml PDGF on day 13. Control organoids (left) have isolated regions with relatively thin collagen fibers (shown in blue). In contrast, the TGFβ1 or PDGF-treated organoids form a network of thick collagen fibers that extend throughout the entire organoid. Collagen producing cells (green) can also be seen in these images. Scale bars, 50 μ. *Bottom:* A quantitative comparison of collagen fiber area in SHG images was performed for control, TGFβ1- or PDGF-treated hepatic organoids ($n = 5$ per measurement) on day 21. There is a statistically significant increase in total collagen abundance (collagen fiber area=total area with collagen fibers/area of the imaged organoids) in the organoids after exposure to TGFβ1 (*, $p < 0.05$) or PDGF (**, $p < 0.01$, Welch t-test). There was also a statistically significant increase in the abundance of thick collagen fibers (i.e., those fibers > 3 um diameter) in the TGFβ1 and PDGF-treated hepatic organoids.

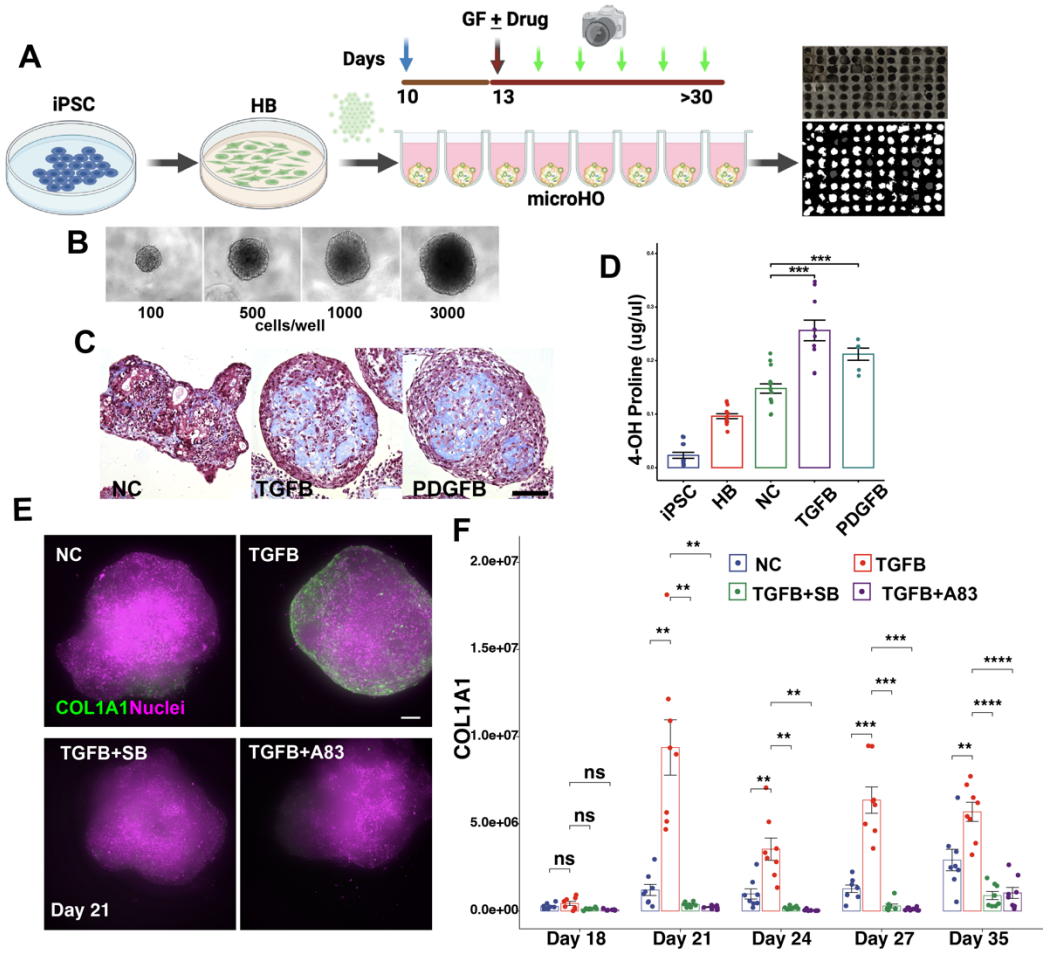

Figure 2. (**A**) A diagram of the HCS platform used for analysis of microHOs. COL1A1-P2A iPSCs are differentiated into hepatoblasts (HB), and 10,000 HBs are placed in each microwell on day 10. Growth factors (GF) and/or drugs are added on day 13, and the cultures are differentiated into hepatic organoids. Culture fluorescence is serially assessed to measure the number of COL1A1-producing cells in the microHO. Bright field (top) and fluorescence (bottom) images of a microwell plate with microHOs is shown on the right. (**B**) A cell number titration experiment was performed by adding the indicated numbers of HBs to microwells and the cells were differentiated through day 12. Bright field images on day 12 reveal that microHOs have a uniform shape and their size is dependent upon the number of input cells. (**C**) Trichrome staining reveals a marked increase in collagen (blue areas) in PDGF or TGFβ-treated microHOs relative to control (NC) microHOs. Scale bar, 50 um. (**D**) The 4-Hydroxy-proline (4OH-Proline) concentration was measured in differentiating HO cultures (iPSC, day 9 HB); and in day 21 control (NC), PDGF- or TGFβ-treated HOs. The bar graph shows the mean ± SE of measurements performed on a total of 15 HOs, which were generated in two separate experiments. There was a significant increase in 4-OH-Proline in the PDGF- or TGFβ-treated

day 21 HOs (***, $p < 0.001$ vs NC, t-test). (**E**) Maximum intensity projection (MIP) images of z stack sections obtained from the indicated type of microHOs on day 21. Scale bar 100 um. Clover expression is green, and nuclei stained with Hoechst 33342 are purple. (**F**) TGFβ1-induced fibrosis in microHOs is blocked by TGFRβ1 inhibitors. COL1A1-P2A Clover HOs were formed by adding 10,000 HBs to each microwell. Then, either nothing (NC), or 50 ng/ml TGFβ1 $\pm$ 10 uM TGFRβ1 inhibitors (SB431542 (SB) or A83-01 (A83)) was added to each microwell on day 13. The amount of $COL1A1^+$ cells within a microHO were serially measured on days 18 through 35. Each dot represents a measurement made on one microHO, and 8 microHOs per treatment were assessed per condition. The significance indicators are ns, not significant; *, $p<0.05$; **, $p<0.01$; ***, $p<0.001$ or ****, $p<0.0001$ for measurements in TGFβ1 treated vs NC microHOs; and for microHOs that were treated with TGFβ1 and drug, the p-values are calculated relative to the TGFβ1 treated microHOs. A two-way ANOVA indicates that drug treatment and time are two variables that have a significant interaction on the fluorescence measurements ($p=1.66 \times 10^{-15}$) (**Table S10**).

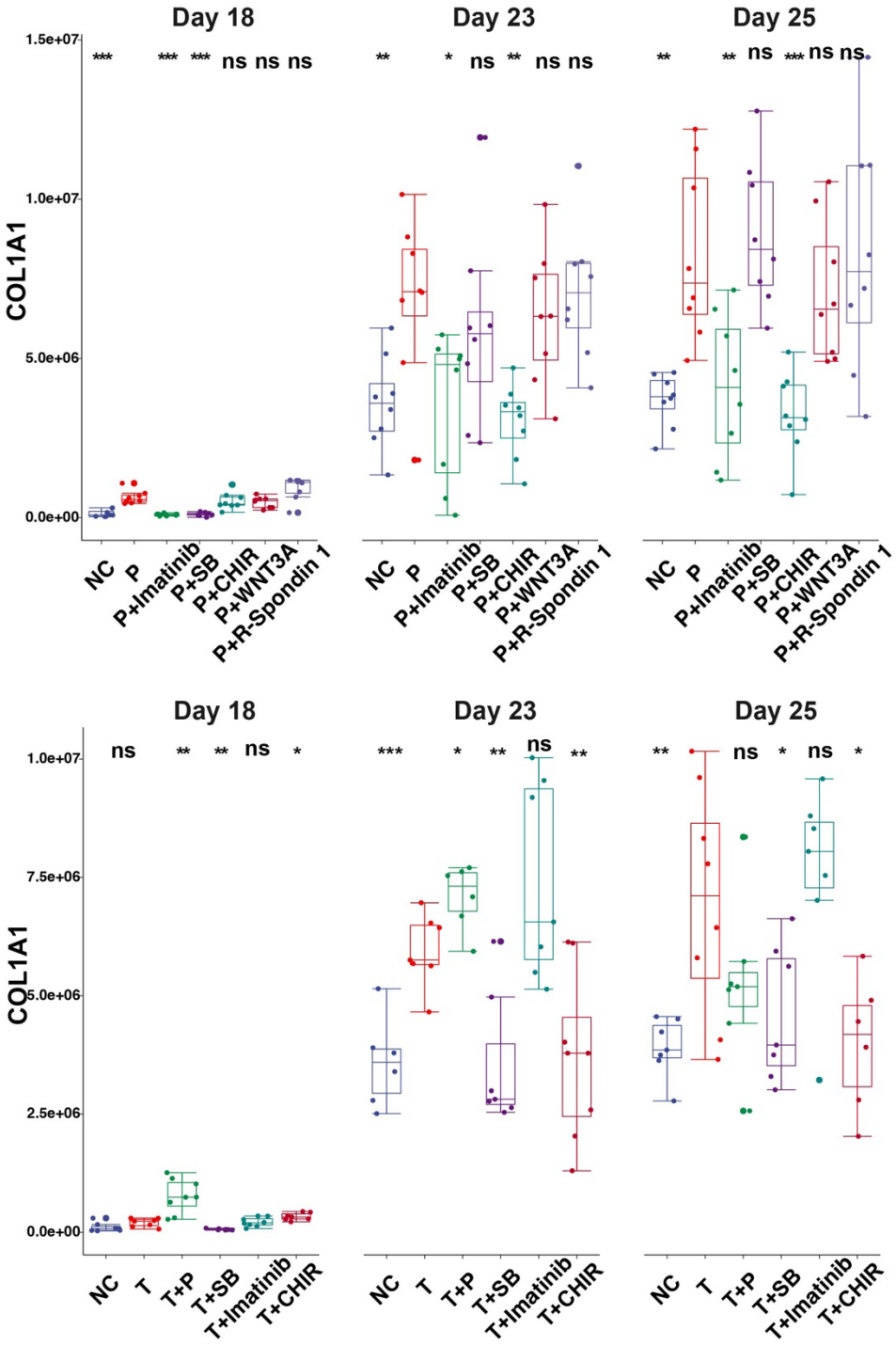

Figure 3. *Top:* The PDGFβ-induced increase in COL1A1^{+} cells is blocked by PDGFRβ and GSK3β inhibitors. *COL1A1*-P2A Clover HOs were formed by adding 10,000 cells from day 9 organoid cultures to each microwell. Then, either nothing (NC), 50 ng/ml PDGFβ (P) or 50 ng/ml PDGFβ with 10 μM imatinib, 10 uM SB431542 (SB), 10 uM CHIR99021 (CHIR), 100 ng/ml

Wnt3a or 100 ng/ml R-spondin 1 was added to each microHO on day 13. *Bottom:* The TGFβ1 induced increase in COL1A1$^+$ cells was blocked by TGFRβ and GSK3β inhibitors. Either nothing (NC), 50 ng/ml TGFβ1 (T), 50 ng/ml TGFβ1 with 50 ng/ml PDGF (T+P), or 50 ng/ml TGFβ1 and either 10 μM imatinib, 10 uM SB431542 (SB), or 10 uM CHIR99021 (CHIR) was added to each microHO on day 13. microHO fluorescence, which indicates the amount of COL1A1$^+$ cells, was serially measured on days 18 through 25. Each dot represents a measurement made on a microHO, the thick line is the median for 8 microHOs that were assessed, and the box plot shows the 25 to 75% range for the measurements. In the panels: ns, not significant; *, $p<0.05$; or **, $p<0.01$, ***, $p<0.001$ for the measurement relative to the value in the NC; or when growth factors or inhibitors were added, the p-values were calculated relative to that of the PDGFβ or TGFβ1 treated cultures. A two-way ANOVA indicates that drug treatment and time are two variables that have a significant interaction on the fluorescence measurements (Table S10).

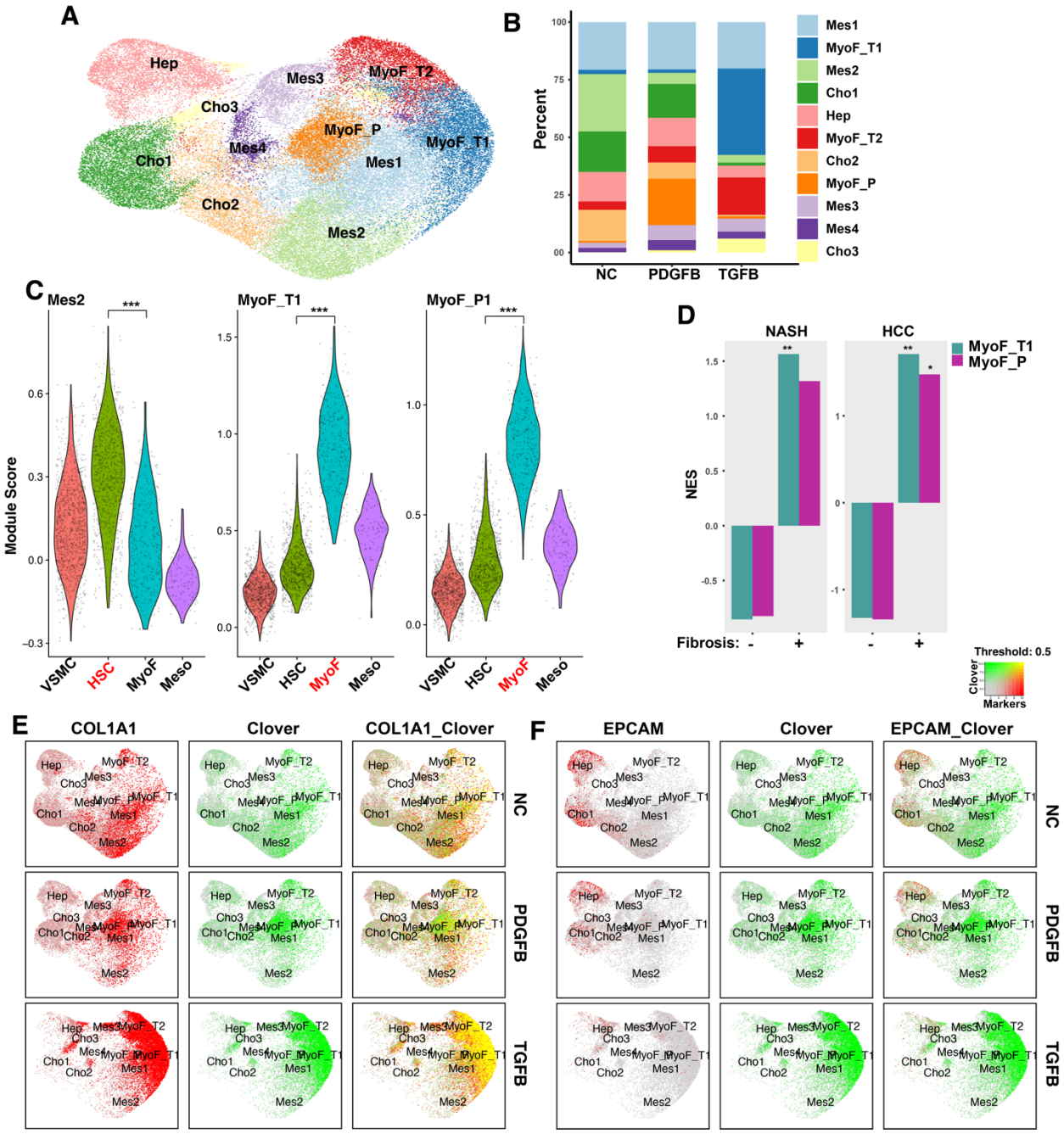

Figure 4. (**A**) A combined sample u-MAP plot shows scRNA-seq data obtained from the cells in day 21 control (NC), PDGFβ- (P) or TGFβ1 (T)-treated microHO cultures. (**B**) The percentages of the 11 different clusters identified by K-nearest neighbor analysis of the scRNA-Seq data shown in (A) are graphed. Each cluster is indicated by a different color and the cell types for each cluster were annotated based upon the genes shown in Table S2. The hepatocyte (Hep) and cholangiocyte (Cho1-3) clusters are indicated. There are four mesenchymal clusters (Mesen1-4): Mes1 is abundant in all three types of organoids, while Mes2 abundance is

increased in PDGFβ-treated microHOs. There are three myofibroblast-like clusters (MyoF_T1, MyoF_T2, MyoF_P), and the abundance of MyoF_T1 and MyoF_T2 cells are markedly increased in TGFβ1-treated microHOs, while the abundance of MyoF_P cells is increased in PDGFβ1-treated microHOs. (**C**) Among the cells in cirrhotic human liver, the MyoF_T1 and MyoF_P transcriptomes are most similar to that of myofibroblasts. The MyoF_T1 or MyoF_P gene signatures were compared with the transcriptomes of the various cell types in cirrhotic human liver tissue (GSE136103 [86]), which include macrophages (MP) and innate lymphoid cells (ILC). The boxplots show that the MyoF_T1 and MyoF_P signatures are most enriched in the myofibroblasts present in cirrhotic human liver tissue. There was a statistically significant difference in the module scores obtained for the various cell types as determined by one-way ANOVA ($p < 0.0001$). The dotted lines represent module scores located 1.5-fold above (or below) (Q3 $\pm$ 1.5 * IQR) interquartile (IQR) range. (**C**) Among the cell types in human liver, the MyoF_T1 and MyoF_P transcriptomes are most similar to myofibroblasts, while Mes2 is most similar to HSC. These violin plots show the results when the Mes2, MyoF_T1, and MyoF_P gene signatures were compared with the transcriptomes of the following cell types in normal and cirrhotic (GSE136103 [86]) human liver: VSMC, vascular smooth muscle; HSC, MyoF; and Meso, mesothelium. Each dot shows the module score of individual cells obtained for each of the four cell types. The MyoF_T1 and MyoF_P module scores are most similar to MyoF, and Mes2 has the most similarity with HSC in human liver. The MyoF module scores for MyoF_T1 and MyoF_P are 3-fold higher ($p<1x10-^{10}$) than that of HSC, and the HSC gene signature module score for Mes2 is 4.8-fold ($p<1x10-^{10}$) higher than for MyoF in human liver. (**D**) The bar graphs show the normalized enrichment score (NES) of the GSEA examining the association of the MyoF_T1 and MyoF_P gene signatures with liver tissue obtained from non-fibrotic (stage 1) or fibrotic (stage 4) NASH liver (GSE135251), and with resected hepatocarcinoma (HCC) tissue that was classified as non-fibrotic or fibrotic (GSE6764). The false discovery rate (FDR) p-value is indicated by the symbol above each bar: *, $P < 0.05$; **, $P<0.01$. The MyoF_T signature was strongly associated with fibrotic NASH liver; and both signatures were strongly associated with fibrotic HCC tissue but not with non-fibrotic NASH or HCC tissue. (**E, F**) Feature plots show the level of expression of *COL1A1* and *Clover* mRNAs (D), or *EPCAM* and *Clover* mRNAs (E) in the u-MAP plot shown in (A). As shown in the color threshold diagram, dot colors represent level of expression of the mRNAs. *COL1A1 and Clover* mRNAs have an overlapping expression pattern; they are predominantly expressed in myofibroblasts, and in mesenchymal cells. In contrast, *EPCAM* mRNA is expressed in hepatocyte and cholangiocyte clusters; and *EPCAM* mRNA expression does not overlap with that of *Clover* mRNA.

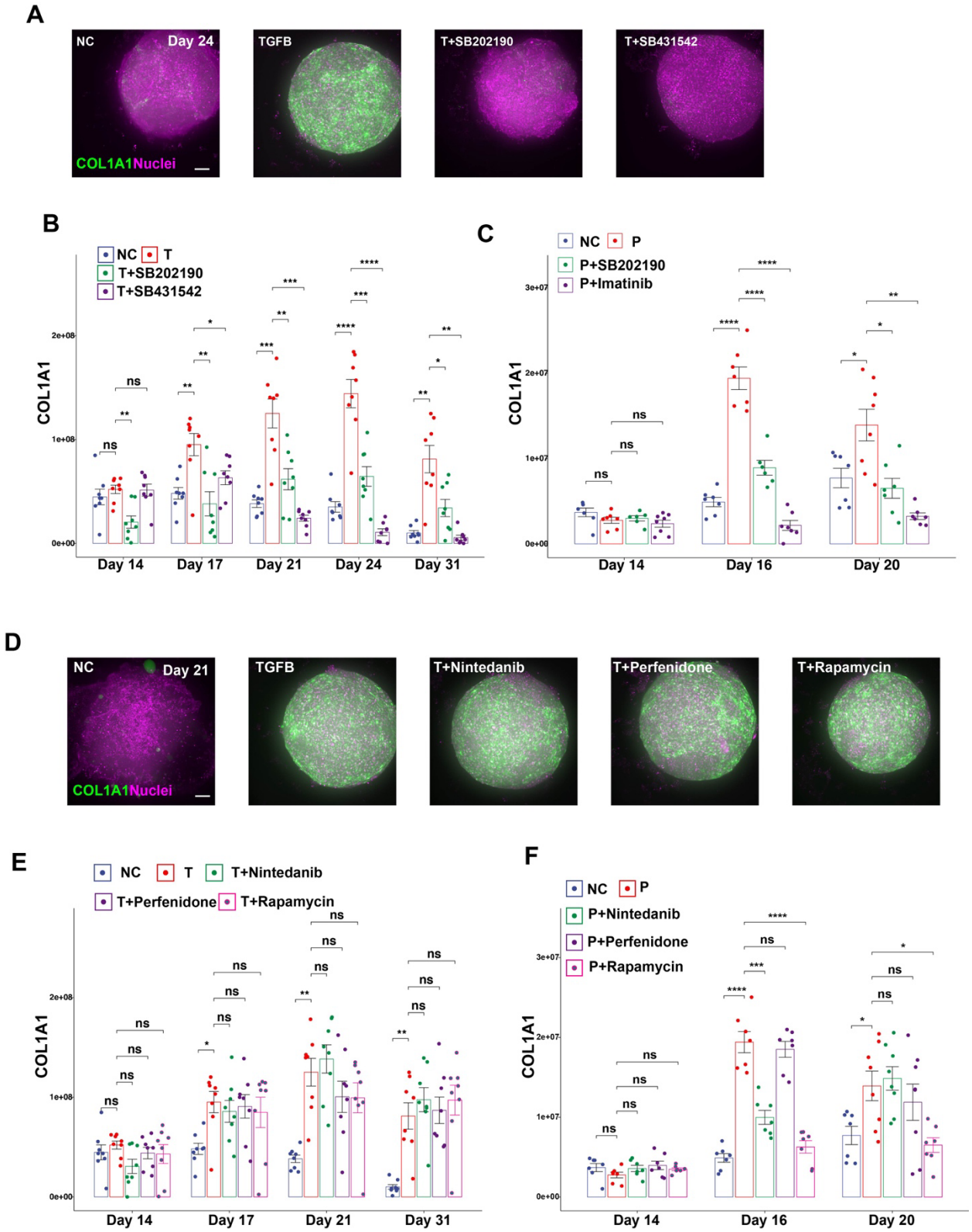
A
NC
Day 24
COL1A1Nuclei
TGFB
T+SB202190
T+SB431542
B
NC
T
T+SB202190
T+SB431542
COL1A1
Day 14
Day 17
Day 21
Day 24
Day 31
C
NC
P
P+SB202190
P+Imatinib
COL1A1
Day 14
Day 16
Day 20
D
NC
Day 21
COL1A1Nuclei
TGFB
T+Nintedanib
T+Perfenidone
T+Rapamycin
E
NC
T
T+Nintedanib
T+Perfenidone
T+Rapamycin
COL1A1
Day 14
Day 17
Day 21
Day 31
F
NC
P
P+Nintedanib
P+Perfenidone
P+Rapamycin
COL1A1
Day 14
Day 16
Day 20

Figure 5. TGFβ1- or PDGF-induced fibrosis in microHOs is inhibited by a p38 MAPK (SB202190) inhibitor (A-C); but only the PDGF-induced fibrosis is inhibited by pirfenidone or rapamycin (D-F). *COL1A1*-P2A Clover microHOs were formed by adding 10,000 HBs to each microwell. Then, either nothing (NC), 50 ng/ml TGFβ1 (T) or 50 ng/ml (PDGF) was added on day 13 to each microwell in the presence or absence of 10 uM of the following drugs: SB431542 (TGFRβ inhibitor), SB202190 (p38 α inhibitor), nintedanib, pirfenidone or rapamycin. (A, D) Maximum intensity projection (MIP) images of z stack sections obtained from microHOs treated with no addition (NC), or 50 ng/ml TGFβ ± 10 uM of the indicated drugs. Scale bar 100 um. Clover expression is green, and nuclei stained with Hoechst 33342 are purple. (B-C, E-F) The amount of $COL1A1^+$ cells within a microHO was serially measured on days 14 through 31. Each dot represents a measurement made on a microHO, the thick line is the median of 8 microHOs that were assessed, and the box plot shows the 25 to 75% range for all measurements per condition. When only growth factors were added, the p-values were relative to the NC, and the significance indicators are ns, not significant; *, $p<0.05$; **, $p<0.01$; ***, $p<0.001$ or ****, $p<0.0001$. When growth factors and inhibitors were added, the p-values were calculated relative to the PDGFβ or TGFβ1 treated microHOs (without added drug). A two-way ANOVA analysis indicates that drug treatment and time are two variables that have a significant interaction on the fluorescence measurements (Table S10).

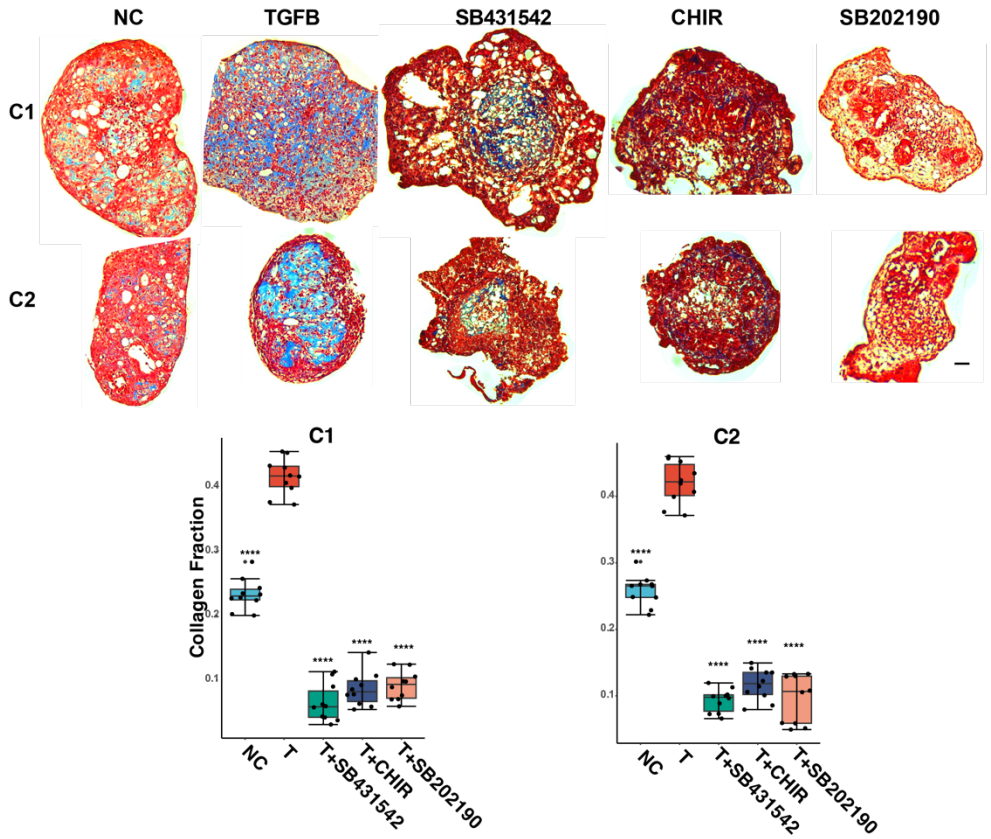

Figure 6. Anti-fibrotic drugs inhibit fibrosis in microHOs produced from iPSC of different genetic backgrounds. microHOs produced from iPSC lines generated from two donors (C1, C2) [11] were treated with no addition (NC), TGFβ (T) (50 ng/ml), or TGFβ and one of the following drugs on day 13: TGFBR inhibitor (10 μM SB431542), GSK3β inhibitor (3 μM CHIR) or a p38 inhibitor (10 μM SB202190). The microHOs were analyzed by trichrome staining on day 21. **(A)** Images of trichrome-stained TGFβ-treated microHOs show a marked increase in collagen-rich connective tissue (blue stained regions) relative to control (NC) microHOs, which only had a thin layer of connective tissue. The TGFβ-induced increased in collagen was markedly inhibited by addition of the TGFBR, GSK3β, or p38 inhibitors. The scale bar on the left: 50 μm. (**B**) Boxplots show the area in microHOs that received indicated treatments (n=6-9 per group) occupied by collagen (collagen fraction). The means for each group were compared using a one-way ANOVA and Tukey's post-test: ****, $p<0.0001$ (for T vs NC, or T vs T+drug).

Supplemental Information

Characterization of Pro-Fibrotic Signaling Pathways in Human Hepatic Organoids

Supplemental note 1: *Supplemental Note 1*: Gene Set Enrichment Analysis (**GSEA**) [1] was used to investigate whether microHOs fibrosis resembled two commonly occurring forms of human liver fibrosis. To do this, genes whose expression levels were increased in MyoF_T1 (n=527) or MyoF_P (n=1716) relative to Mes2 were used to form myofibroblast-specific gene expression signatures. GSEA calculates a normalized expression score (**NES**), which indicates whether the signature genes were enriched in fibrotic or non-fibrotic liver tissue. GSEA was first performed using expression data obtained from early (non-fibrotic) stage 1 and late (fibrotic) stage 4 NASH liver tissue (GSE13525 [2]). Liver fibrosis develops as NASH liver disease advances; myofibroblast activation is key to its pathogenesis [3-5]; and the extent of liver fibrosis is the major determinant of NASH outcome [6, 7]. GSEA results indicate that the MyoF_T1 (NSE 1.56; false discovery rate (FDR) 0.0178) gene expression signature was very strongly associated with stage 4 NASH, but not with early (NES -0.85 FDR 1) stage 1 NASH liver (**Fig. S10A, Table S9)**). The MyoF_T1 (NES 1.71, FDR 0.005) signature was also associated with liver fibrosis caused by hepatocellular carcinoma, whereas it (NES -1.32, FDR 0.17) was not associated with non-fibrotic hepatocarcinoma liver tissue (GSE6764 [8]) (**Fig. S10B**). In contrast, The MyoF_P signature had a positive (but not statistically significant association) with stage 4 NASH (NES 0.45, FDR 0.14) and HCC-induced liver fibrosis (NES 0.36 FDR 0.06). Thus, GSEA analyses indicate that the MyoF_T1 signature in microHOs resemble those in two commonly occurring types of human liver fibrosis.

Supplemental note 2: *Interactions between the TGFβ, Wnt/β-catenin and p38 MAPK pathways*. The TGFβ1 and Wnt/β-catenin pathways have several interaction points. (i) TGF-β significantly enhances hepatic WNT-5A expression *in vivo* and in myofibroblasts *in vitro* [9]. (ii) The interdomain regions of SMAD transcription factors have two residues that are phosphorylated by GSK3β in the nucleus, and their phosphorylation state regulates SMAD transcriptional activity and turnover [10]. Hence, the ability of the GSK3β inhibitor to block TGFβ1-induced fibrosis in microHOs could (at least in part) be mediated by altering the phosphorylation state of these two sites, which could alter SMAD transcription factor activity. (iii) During development, receptor tyrosine kinase and Wnt/β-catenin pathway signals were shown to be integrated by the level of SMAD phosphorylation [11].

The Wnt/β-catenin and p38 MAPK pathways also interact at several nodes. (i) Wnt ligands have been shown to activate p38 MAPK activity [12]. (ii) GSK3β phosphorylation by p38 MAPK regulates its kinase activity. MAPK kinases have a Thr–Gly–Tyr dual phosphorylation motif within their kinase activation loop, and both sites must be phosphorylated to fully activate the kinase. The MAP2K kinases MKK3 and MKK6 are the major upstream kinases for p38 activation [13]. However, phosphorylation on Ser^{389} on GSK3β is a major mechanism for downregulating its kinase activity and p38α was shown to inactivate GSK3β by this mechanism: p38-mediated phosphorylation of Ser^{389} on GSK3β was shown to cause β-catenin accumulation and activation of the Wnt signaling pathway [12, 14]. By this mechanism, p38 MAPK inhibitors could reduce Wnt pathway activation, which could prevent the development of a fibrosis that was dependent upon Wnt signaling.

Materials and Methods

Chemicals. The growth factors, drugs, antibodies, and other staining reagents are shown in Tables S6-S7.

iPSCs and HO generation. The human iPSC line (C3) used in this study was prepared as previously described [15]. The biopsy sample used to generate this iPSC line was obtained according to a protocol (number 10368) approved by the Institutional Review Board at Stanford. The CRISPR-assisted insertion tagging system (CRISPaint) [16] plasmid (pCRISPR-HOT-Clover-BlastR) was obtained from Addgene (Plasmid #138569; http://n2t.net/addgene:138569). A clover expression cassette (**P2A-Clover**) was inserted at the COOH terminus of the endogenous *COL1A1* gene of the iPSC line without a STOP code using a sgRNA (TTGGGATGGAGGGAGTTTAC). After Blasticidin selection, colonies obtained from single cells were picked and genotyped for the correct in-frame insertion using forward (actcccacgtggtaatgccc); and reverse (cttcagggtcagcttgccg) primers. iPSCs were differentiated into hepatic organoids (HOs) via culture in a series of media containing different growth factors using previously described methods [15].

Second Harmonic Generation (SHG) microscopy. SHG (collagen fibers) images from day 21 control, PDGF-treated and TGFβ1-treated HOs were collected on a multimodal nonlinear optical microscope setup, consisting of a modified inverted confocal microscope (Nikon, Ti2-E with C2 scanner and 60X water immersion objective, NA=1.27) and a picosecond-pulsed laser source (APE picoEmerald S, 2 ps pulse width, 80 MHz repetition rate, and 10 cm^{-1} bandwidth). As previously described[15], SHG data collection was made in the epi-direction with two narrow

bandpass filters (Semrock FF01-400/12, Thorlabs MF390-18) and one shortpass filter (Thorlabs FESH0500). For the quantitative analyses, the area of the collagen fibers (identified by Otsu thresholding) was calculated for each SHG image and divided by the total sample area, forming the collagen area fraction (in %). To determine the diameter of the collagen fibers, the local thickness of the fibers was evaluated by applying the ImageJ Local Thickness routine (see the Analyze menu in Fiji) [17] to the SHG data. The volume fraction of thick collagen fibers (diameter ≥ 3 μm) was estimated by dividing the number of pixels represented by local thickness values ≥ 3 μm by the total number of pixels of the stack. To test whether the volume fractions obtained for control and TGFβ1- or PDGF-treated organoids were significantly different, the Welch's t-test was applied (* $p<0.05$ and ** $p<0.01$).

microHO generation. To produce microHOs, 50~60% confluent iPSC cultures were switched to an endoderm differentiation medium that consisted of DMEM/F12 + ITS (GIBCO) supplemented with 0.1 mM nonessential amino acids, 1 mM pyruvate and 2 mM L-alanyl-L-glutamine dipeptide (GlutaMAX). On days 1 to 2, 100 ng/ml Activin-A (Peprotech, Rocky Hill, NJ), 10 ng/ml BMP4 (Peprotech), 100 ng/ml bFGF (Peprotech), 3 mM CHIR99021 (Selleckchem, Houston, TX) and 10 uM LY294002 (Selleckchem) were added this medium. On day 3, 100 ng/ml Activin-A and 100 ng/ml bFGF were added the definitive endoderm differentiation medium. From days 4 to 9, 20 ng/ml FGF10 (Peprotech) and 20 ng/ml BMP4 were added to the hepatoblast medium, which consisted of which consisted of Advanced RPMI 1640 Medium (Gibco) that was supplemented with GlutaMAX and ITS. After day 9, the hepatoblasts were dissociated to single cells in Accutase (Invitrogen) medium with 10 uM Y-27632 (Santa Cruz Biotechnology, Dallas, Texas). Then, 1000 to 5000 cells/well were re-aggregated in low-cell-adhesion Nunclon™ Sphera™ 96 well Microplates (ThermoFisher) that contained serum-free HO growth and differentiation medium, which consisted of William's E medium supplemented with 0.1% Polyvinyl alcohol (Sigma-Aldrich), 0.1 mM nonessential amino acids, 1 mM pyruvate, 2 mM L-alanyl-L-glutamine dipeptide (GlutaMAX), 10 mM Y-27632, 100 ng/ml EGF, 10 ng/ml HGF, 10 μM Dexamethasone and 10 μM Hydrocortisone (Sigma, St. Louis MO). On day 13, 50 ng/ml of TGFβ1 (Peprotech, 100-21; or Sinobiological, 10804-HNAC) or 50 ng/ml of PDGFB (Miltenyibiotec, 130-108-163; or Peprotech, 100-14B) was added to each microwell.

microHO analysis. For COL1A1^{+} and Hoechst 33342 (Invitrogen, H3570) fluorescence measurements, 3D stacked images were captured from day 14 to day 31 cultures using a

Molecular Devices ImageXpress Micro Confocal system. For confocal imaging20 to 40 planes crossing the whole organoid at 20 um intervals were captured using a 10X 0.45 Plan Apo 4mm WD objective with a 60-um pinhole. For each 10X confocal z-stack field (enough to cover one whole organoid), maximum intensity projections (MIPs) were generated from all of the acquired z-planes (the number planes ranged from 20 to 40 depending on the batch size). MIPs from each channel belonging to the same well were used for organoid segmentation and feature extraction by applying the machine learning based 'Trainable Weka Segmentation' [18] plugin from FIJI [19]. Each individual organoid edge was automatically segmented based on the nuclei signal (Hoechst 33342). Cell numbers were determined using the 'Find Maxima' function in defined area of an organoid after segmentation. COL1A1-P2A-Clover^{+} cells were segmented based on fluorescence. For training purposes, each analyzed element in every image (total 12 images) were used to train the classifiers by manual labelling all positive spots. Then, for experimental image analysis, the saved classifier was used to generate the probability map for each image. Segmented areas were then isolated, thresholded and binarized, and the Integrated Density was calculated from segmented area. An unpaired Student's t-test was used to test whether the measurements were significantly different between each comparison group. The macro script used for this analysis is available upon request.

Immunohistochemistry. Fresh organoids were harvested and fixed in 4% paraformaldehyde for 30 minutes. All organoids were either stained directly or embedded in low melting point agarose (IBI Scientific, Dubuque, Iowa). The primary antibodies used for staining are listed in Table S5. The organoids were stained with the primary antibody, and permeabilized by incubation with 1% Triton X-100 (Sigma-Aldrich, St. Louis, MO) and 10% chicken serum (Jackson ImmunoResearch, Bar Harbor, MA) overnight. Then, secondary antibody-staining was performed using an Alexa Fluor labeled chicken anti IgG (H+L), which was cross-adsorbed with a secondary antibody in 10% chicken serum (Invitrogen, Pleasanton, CA).

4-hydroxyproline quantitation. iPSC and day 9 hepatoblast cultures and day 21 control, PDGF- or TGFβ-treated HOs (n=16 per condition) were isolated and snap frozen in liquid nitrogen. 4-hydroxy proline levels were measured using the Hydroxyproline Assay kit (Sigma, MAK008) according to the manufacturer's instructions. In brief, HOs were homogenized in 100 µL of water and transferred to a pressure-tight polypropylene vial. Then, 100 µL of concentrated hydrochloric acid (HCl,12 M) was added, a cap was placed on tightly on the vial, and the sample was hydrolyzed at 120°C for 3 hours. The hydrolysate was centrifuged at 10,000 × g for 3

minutes. The clear supernatant was transferred and used for colorimetric assay of 4-hydroxyproline, which was performed according to the manufacturer's instructions.

Trichrome staining. Day 21 control, PDGF- or TGFβ- (+ drug) treated organoids were harvested, allowed to settle by gravity, and were embedded in low melting point agarose (IBI Scientific, Dubuque, Iowa). The embedded organoids were then processed by sectioning of the paraffin-embedded tissue to produce 10-micron tissue sections. To assess the amount of collagen in the organoids, trichrome staining of the tissue sections was performed using the MASSON'S 2000 TRICHROME STAIN KIT according to the manufacturer's instructions.

Immunoblotting. iPSCs and day 9 hepatoblast cultures, and day 21 control, PDGF- or TGFβ-treated HOs (n=16 per condition) were lysed in RIPA buffer. The lysates were analyzed by PAGE on a 4-15% Tris-glycine gel. After blotting onto a membrane, the membranes were incubated with a 1:2000 dilution of an anti-GFP antibody (Clontech 632381, clone JL8) for detection of Clover protein, and the secondary antibodies were IRDye® 680 and 800 (LI-COR Biosciences).

scRNA-Sequencing. Control, PDGFB- or TGFβ1-induced microHOs (n>30 per group) were harvested from multiple independently prepared sets of cultures, and single cell suspensions were prepared by protease digestion as described [15]. The single cell suspensions were visually inspected under a microscope, cells were counted using a Scepter™ 2.0 Handheld Automated Cell Counter (EMD Millipore, Burlington, MA), and then resuspended in PBS with 0.01% BSA. scRNA-seq libraries were prepared by using the spit-pool based scRNA-Seq method (Evercode™ WT Mini v2 from Parse biosciences) according to the manufacturer's instructions. In brief, ~5,000 cells from each group were split into 3 wells for the first round of sample barcoding, and the final pooled cells were divided into two equal libraries for sequencing. The expression matrix was generated using the 'Parse Biosciences analysis pipeline.' A total of 38,716 features that were generated from 13,160 cells were generated from four experimental batches, and 57, 7778 cells were recovered that passed quality control for processing of the scRNA-Seq data.

Flow cytometry iPSCs were dissociated into single cells by incubation with 5 μM ETDA (Invitrogen) in PBS; and hepatoblasts were dissociated using Accutase (Gibco). Single cell suspensions were prepared from microHOs by protease digestion as described [15]. Flow

cytometry was performed using at a BD Accuri C6 flow cytometer using the conjugated antibodies listed in Table S2, and the data was analyzed using FCS Express (denovosoftware.com) software. A density plot of forward scatter height (FSC-H) vs. forward scatter area (FSC-A) was used to exclude doublets.

***scRNA-Seq data analysis*.** The scRNA-Seq data was imported into 'Seurat' [20] for the subsequent analysis steps. (i) Cells with unique gene counts <200 or where the percentage of mitochondrial mRNAs was >10% were removed. (ii) A total of 2000 variable genes were identified using the default settings. Four batches of data were integrated by standard processing methods using the Seurat integration function. Unwanted sources of variation were removed by regression analysis, which was performed to mitigate the effect of signals caused by mRNAs with unique molecular identifiers and mitochondrial expression. (iii) Ten principal components were used to construct the shared nearest neighbor (SNN) graph, and the parameter regulating the resolution of the 'Find Clusters' program, was set to 0.5. This resulted in the identification of 11 unique clusters for all 57,778 cells. To identify the cell type of each cluster, differentially expressed genes for the pre-defined cell types were computed using the 'FindAllMarkers' function within the Seurat Package with the following parameters: only.pos = TRUE, min.pct = 0.25, logfc.threshold = 0.25. Seurat then identifies the differentially expressed genes using the non-parametric Wilcoxon rank sum test.

Module score calculation. Module scores were calculated to assess the relationship between the transcriptomes of microHO clusters and the different types of cells in human liver tissue. scRNA-Seq data obtained from normal and cirrhotic human liver tissue (GSE136103) [21] was used to identify the different types of liver cells. Differentially expressed genes were calculated for each of the clusters in microHO (MyoF_T1, MyoF_P, Mes2) and human liver tissue (Myofibroblast, HSC, VSMC and Meso), using the 'FindMarkers' function of the R package in Seurat [22]. Then, each of the gene signatures used for determining the module score were selected based on the intersection between the marker genes in microHO and those in the cell types in human liver. There were 53, 84, and 31 shared genes that were used to calculate the module scores for MyoF_T1 vs MyoF in liver, MyoF_P and liver MyoF, and Mes2 and liver HSC, respectively. For comparisons of the scores obtained with vascular smooth muscle cells (VSMC), HSC, Myofibroblasts and Mesothelial cells, a one-way ANOVA was used to compare the means of the measurements for the four groups. The Tukey multiple comparison of the

means test was then used to determine whether there was a significant difference between the means of all possible comparisons.

Gene signature expression analyses (GSEA). The myofibroblast-specific gene expression signatures for genes whose expression was upregulated in MyoF_T1 (n=527) or MyoF_P (n=1716) relative to Mes2 (Table S*) were identified using the '*FindMarkers*' function in '*Seurat*' [20] with the parameter 'min.pct' set at 0.25 (which indicates the minimum fraction of cells within a cluster that expressed a given gene); and the default Wilcoxon rank sum test was used to perform this analysis. Two publicly available gene expression datasets for NASH (GSE135251 [2]) and cirrhotic (GSE6764 [8]) liver were obtained from the Gene Expression Omnibus using the '*GEOquery*' as described [23]. Cirrhotic liver tissue was obtained from 10 subjects undergoing liver resection for hepatocellular carcinoma at one of 3 US or European hospitals; and their liver tissues were classified as cirrhotic by the examining pathologist. The hepatocellular carcinoma samples (HCC) samples examined in this study were obtained from eight subjects whose liver was resected for HCC, but these specimens did not have fibrosis or cirrhosis according to the examining pathologist. The 10 normal liver tissues (used for comparison) were obtained from 10 subjects undergoing liver resection for other reasons at the same hospitals, and their liver tissue was classified as normal by the examining pathologist [8]. For the NASH analysis, 216 liver biopsies were examined by histology, which generated the fibrosis stage scores: 4 biopsies were classified as Stage 4, 48 biopsies were classified as Stage 1, and 46 as stage 0.

The GSEA for the myofibroblast signatures were calculated for the gene expression datasets generated from these samples using previously described methods [1]; and 1000 permutations were used for significance assessment for each analysis. The Enrichment score (ES) reflects the degree to which the Myofibroblast gene set is overrepresented at the top or bottom of a ranked list of genes; the Normalized enrichment score (NES) was used to compare analysis results across gene sets; and the false discovery rate (FDR) was used to estimate the probability that a gene set with a given NES represents a false positive finding.

2-way analysis of variance (ANOVA) calculations. The 2-way ANOVA was used to compare the means of the COL1A1:Clover signal (calculated as area * mean intensity (IntDen)) between the different drug treatment groups and time points, while also assessing interaction effects between the treatment groups and time. The two-way ANOVA was performed using the 'aov'

function of the 'R\stats' package, and both groups and time points were analyzed as categorical independent variables. The null hypothesis was that there is no difference in the means of the different treatment groups or timepoints, and that the treatment groups and time points do not interact in any way. Since the two-way ANOVA of the data shown in Figures 2D, 3A, 3B, 5B, and 5C use separate datasets, a correction for multiple testing is not needed.

Analysis of drug effect in C1 and C2 microHOs. The C1 and C2 iPSC lines were generated and characterized as previously described [15] and used to prepare microHOs as described above. Trichrome staining of day 21 microHOs was performed according to the manufacturer's instructions using MASSON'S 2000 TRICHROME stain (Americanmastertech, Lodi, CA). Image segmentation and quantitative measurement of collagen rich areas was performed using our previously described methods [24]. In brief, Fiji (2.1.0) implementation of ImageJ was used to quantify the areas of positive staining. The 'Trainable Weka Segmentation' plug-in was used to train the classifiers and calculate the test experimental image. Statistical analysis was performed using a one-way ANOVA to assess the overall differences between group means, and Tukey's post-test was then used for pairwise comparisons to identify groups with significant differences in their means.

References

[1] Subramanian A, Tamayo P, Mootha VK, Mukherjee S, Ebert BL, Gillette MA, et al. Gene set enrichment analysis: a knowledge-based approach for interpreting genome-wide expression profiles. Proc Natl Acad Sci U S A 2005;102:15545-15550.
[2] Pfister D, Nunez NG, Pinyol R, Govaere O, Pinter M, Szydlowska M, et al. NASH limits anti-tumour surveillance in immunotherapy-treated HCC. Nature 2021;592:450-456.
[3] Tsuchida T, Friedman SL. Mechanisms of hepatic stellate cell activation. Nature reviews Gastroenterology & hepatology 2017;14:397-411.
[4] Sircana A, Paschetta E, Saba F, Molinaro F, Musso G. Recent Insight into the Role of Fibrosis in Nonalcoholic Steatohepatitis-Related Hepatocellular Carcinoma. International journal of molecular sciences 2019;20.
[5] Marcher AB, Bendixen SM, Terkelsen MK, Hohmann SS, Hansen MH, Larsen BD, et al. Transcriptional regulation of Hepatic Stellate Cell activation in NASH. Sci Rep 2019;9:2324.
[6] Tanaka N, Kimura T, Fujimori N, Nagaya T, Komatsu M, Tanaka E. Current status, problems, and perspectives of non-alcoholic fatty liver disease research. World J Gastroenterol 2019;25:163-177.
[7] Angulo P, Kleiner DE, Dam-Larsen S, Adams LA, Bjornsson ES, Charatcharoenwitthaya P, et al. Liver Fibrosis, but No Other Histologic Features, Is Associated With Long-term Outcomes of Patients With Nonalcoholic Fatty Liver Disease. Gastroenterology 2015;149:389-397 e310.
[8] Wurmbach E, Chen YB, Khitrov G, Zhang W, Roayaie S, Schwartz M, et al. Genome-wide molecular profiles of HCV-induced dysplasia and hepatocellular carcinoma. Hepatology 2007;45:938-947.

[9] Beljaars L, Daliri S, Dijkhuizen C, Poelstra K, Gosens R. WNT-5A regulates TGF-beta-related activities in liver fibrosis. Am J Physiol Gastrointest Liver Physiol 2017;312:G219-G227.
[10] Macias MJ, Martin-Malpartida P, Massague J. Structural determinants of Smad function in TGF-beta signaling. Trends Biochem Sci 2015;40:296-308.
[11] Fuentealba LC, Eivers E, Ikeda A, Hurtado C, Kuroda H, Pera EM, et al. Integrating patterning signals: Wnt/GSK3 regulates the duration of the BMP/Smad1 signal. Cell 2007;131:980-993.
[12] Bikkavilli RK, Feigin ME, Malbon CC. p38 mitogen-activated protein kinase regulates canonical Wnt-beta-catenin signaling by inactivation of GSK3beta. J Cell Sci 2008;121:3598-3607.
[13] Zarubin T, Han J. Activation and signaling of the p38 MAP kinase pathway. Cell Res 2005;15:11-18.
[14] Thornton TM, Pedraza-Alva G, Deng B, Wood CD, Aronshtam A, Clements JL, et al. Phosphorylation by p38 MAPK as an alternative pathway for GSK3beta inactivation. Science 2008;320:667-670.
[15] Guan Y, Xu D, Garfin PM, Ehmer U, Hurwitz M, Enns G, et al. Human Hepatic Organoids for the Analysis of Human Genetic Diseases. JCI Insight 2017;2:pii: 94954.
[16] Schmid-Burgk JL, Honing K, Ebert TS, Hornung V. CRISPaint allows modular base-specific gene tagging using a ligase-4-dependent mechanism. Nature communications 2016;7:12338.
[17] Hildebrand T, Ruegsegger P. A new method for the model-independent assessment of thickness in three-dimensional images. J of Microscopy 1996;185:67-75.
[18] Arganda-Carreras I, Kaynig V, Rueden C, Eliceiri KW, Schindelin J, Cardona A, et al. Trainable Weka Segmentation: a machine learning tool for microscopy pixel classification. Bioinformatics 2017;33:2424-2426.
[19] Schindelin J, Arganda-Carreras I, Frise E, Kaynig V, Longair M, Pietzsch T, et al. Fiji: an open-source platform for biological-image analysis. Nat Methods 2012;9:676-682.
[20] Butler A, Hoffman P, Smibert P, Papalexi E, Satija R. Integrating single-cell transcriptomic data across different conditions, technologies, and species. Nat Biotechnol 2018;36:411-420.
[21] Ramachandran P, Dobie R, Wilson-Kanamori JR, Dora EF, Henderson BEP, Luu NT, et al. Resolving the fibrotic niche of human liver cirrhosis at single-cell level. Nature 2019;575:512-518.
[22] Hao Y, Stuart T, Kowalski MH, Choudhary S, Hoffman P, Hartman A, et al. Dictionary learning for integrative, multimodal and scalable single-cell analysis. Nat Biotechnol 2023.
[23] Davis S, Meltzer PS. GEOquery: a bridge between the Gene Expression Omnibus (GEO) and BioConductor. Bioinformatics 2007;23:1846-1847.
[24] Guan Y, Enejder A, Wang M, Fang Z, Cui L, Chen SY, et al. A human multi-lineage hepatic organoid model for liver fibrosis. Nature communications 2021;12:6138.

Table S1. Drugs and chemicals used in these studies.

Reagent	Company	Catalog #
palmic acid	SigmaAldrich	P5585
Oleic acid	SigmaAldrich	O1383
Stearic acid	SigmaAldrich	S4751
Myristic Acid	Caymanchem	13351
Myristoleic Acid	Caymanchem	9002461
Palmitoleic Acid	Caymanchem	10009871
Elaidic Acid	Caymanchem	90250
CDCA	SigmaAldrich	C9377
Activin A Protein	Sinobiological	10429-HNAH
Animal-Free Recombinant Human EGF	Peprotech	AF-100-15
EGF	Sinobiological	10605-HNAE
FGF4	Peprotech	100-31
HGF	Sinobiological	10463-HNAS
FGF10	Sinobiological	10573-HNAE
FGF2 Protein, Human, Recombinant	Sinobiological	10014-HNAE
FGF10	Peprotech	100-26
Human PDGF-BB IS	Miltenyibiotec	130-108-163
Human VEGF (165) IS	Miltenyibiotec	130-109-383
Recombinant Human PDGF-BB (carrier-free)	Biolegend	577302
Recombinant Human PDGF-BB	Peprotech	100-14B
Recombinant Human PDGF-BB Protein, CF	rndsystems	220-BB-010In Stock
TGF beta 1 Protein, Human, Rhesus, Cynomolgus, Canine, Recombinant	Sinobiological	10804-HNAC
Recombinant Human BMP-4	Peprotech	120-05
Recombinant Human BMP-4 (carrier-free)	Biolegend	795606
Recombinant Human/Mouse/Rat Activin A	R&D	338-AC-010
Recombinant Human FGF-Basic (146 a.a.)	Peprotech	AF-100-18C
Wnt3a	Peprotech	315-20
OSM	Peprotech	300-10
IL3 Protein, Human, Recombinant (His Tag)	Sinobiological	11858-H08H
IL6	R&D	7270-IL-010/CF
IL-13 Protein, Human, Recombinant	Sinobiological	10369-HNAC
IL-33 Protein, Human, Recombinant	Sinobiological	10368-HNAE
IGF1	R&D	291-G1-200
R-Spondin 1 Protein	R&D	4645-RS
JAG-1 protein	StemRD	Cat#: JAG-1-pep-100
SB202190 (FHPI)	Selleckchem	S1077
SB431542	Selleck	S1067
Sirolimus (Rapamycin)	Medkoo	100766
Imatinib mesylate	Medkoo	100470
DAPT (GSI-IX)	Selleckchem	S2215
LDN-193189	Selleckchem	S2618
SAG	Selleckchem	S7779
IWR1-en	Selleckchem	S7086
A-83-01	Santa Cruz Biotechnology	sc-203791
PI-103	Tocris	2930
PD0325901	Santa Cruz Biotechnology	sc-205427
CHIR99021	Tocris	4423
Wnt-C59	Tocris	5148
BIO	Selleckchem	S7198
Thiazovivin	Medchemexpress	HY-13257
Nintedanib	Tocris	7049
Pirfenidone	Tocris	1093
polyvinyl alcohol	SigmaAldrich	P8136
Matrigel	BD	354234

Table S2. Antibodies and staining reagents used in these studies.

Name	Company	Catalog#	Dilution
CK8	abcam	ab53280	1/100 - 1/250
CK8	DSHB	TROMA-I	200
COL1	ABCAM	ab34710	1:100
GFP Tag Polyclonal Antibody	thermofisher	A-11122	200-2000
GFP Antibody (B-2)	scbt	sc-9996	50
Human Albumin Antibody	Bethyl	A80-129A	1:200 – 1:2,000
PDGFRB	eBioscienc	14-1402-82	100
PDGFRB	ABCAM	ab32570	100
PDGFRB	R&D	AF385-SP	100
PDGFRB	ll Signaling Technolo	3169T	100
LipidSpot™ Lipid Droplet Stains	biotium	#70069-T	
MitoSox Red	Invitrogen	M36008	
Alexa Fluor® 647 anti-human CD326 (EpCAM) Antibody	biolegend	324212	1:20

Cluster	Cell Type	NC (%)	PDGF (%)	TGFβ (%)
0	Mes1	20.7	20.5	20.2
1	MyoF_T1	1.9	1.5	37.5
2	Mes2	24.9	4.8	3.3
3	Cho1	17.6	14.7	1.3
4	Hep	12.8	12.3	5.2
5	MyoF_T2	3.6	7.07	16.2
6	Cho2	13.5	7.1	0.7
7	MyoF_P	0.8	20.1	1.0
8	Mes3	2.2	6.5	5.7
9	Mes4	1.9	4.4	3.0
10	Cho3	0.1	1.0	6.0

Table S3. The cell types and the percentage of the total number of cells in the 11 cell clusters identified by analysis of scRNA-Seq data in day 21 control, PDGF-, and TGFβ1-treated microHOs are shown. The transcriptomes of the 10 other cell clusters in the day 21 microHOs were defined using canonical markers and by comparison with the cells in control and cirrhotic human livers. Based upon the expression of canonical mRNAs and level of concordance between the cell cluster transcriptomes and the cell types identified in human liver, the microHOs have cholangiocytes (Cho1-3), hepatocyte (Hep), mesenchymal cell (Mes1-4) and myofibroblast (MyoF_T1-2, MyoF_P) clusters. A myofibroblast cluster (MyoF_T1) was far more abundant in the TGFβ1-treated microHOs than in control or PDGF-treated microHOs (37.5% of total vs <2%), while another myofibroblast cluster (MyoF_P) was more abundant in the PDGF-treated microHOs than in control or TGFβ1-treated microHOs (20% vs <2% of the total number of cells).

Table S4. The cell types for the 11 cell clusters were determined by analysis of the differentially expressed genes (shown in table S5) identified for each cluster. Selected mRNAs that are representative of the identified cell type for each cluster are shown.

Cluster	Marker mRNAs
Mes1	*COL14A1, ADAMTS1, DLK1, PDGFA, DPP, LUM*
MyoF_T1	*ACTA2, CLIP, TIMP3, ITGA11, COL1A1, TIMP1, ATCB2*
Mes2	*CNTN5, COL11A1, KDR*
Cho1	*KRR19, KRT7, SOX9, EPCAM*
Hep	*AFP, FGB, APOB, CKB, CFTR, CDH17, ALB, SERPINA1*
MyoF_T2	*COL1A1, ACTA2, C3, KLF3, FLNC*
Cho2	*KRR19, KRT7, SOX9, EPCAM*
MyoF_P	*PAPPA, COL1A1, ACTA2*
Mes3	*NCAM1, VIM, PDGFRA, PDGFRB, CXCL14*
Mes4	*NCAM1, VIM, PDGFRA, PDGFRB, MKI67*
Cho3	*KRR19, KRT7, SOX9, EPCAM*

Table S5 is provided at the end of this file.

Table S6. The results of 1-way ANOVA analyses of the cell percentages calculated by analysis of the scRNA-Seq data for the five biological replicates from the control, PDGF- and TGFβ-treated microHO preps shown in Figure S8. The degrees of freedom (DF), the sum of the squares (Sum Sq) and mean squared (mean Sq) of the variance, calculated F-value, and the probability Pr(>F) from the ANOVA are shown. A Pr(>F) < 0.05 indicates that there was a significant effect of the indicated variable. There were significant differences in the % of MyoF_T1, Mes2, MyoF_P and Cho3 cells as indicated by the p-value: ***; 0.001, **; 0.01, *; 0.05. However, Cho3 abundance was ≤1% in all three types of microHOs.

	Df	Sum Sq	Mean Sq	F value	Pr(>F)	
Mes1	2	5	2.6	0.009	0.991	
Residuals	12	3599	299.9			
	Df	Sum Sq	Mean Sq	F value	Pr(>F)	
MyoF_T1	2	1259	629.7	6.046	**0.0153**	*
Residuals	12	1250	104.1			
	Df	Sum Sq	Mean Sq	F value	Pr(>F)	
Mes2	2	747.4	373.7	8.941	**0.00419**	**
Residuals	12	501.6	41.8			
	Df	Sum Sq	Mean Sq	F value	Pr(>F)	
Cho1	2	339.8	169.92	1.946	0.185	
Residuals	12	1047.8	87.32			
	Df	Sum Sq	Mean Sq	F value	Pr(>F)	
Hep	2	134.6	67.28	0.974	0.405	
Residuals	12	828.7	69.05			
	Df	Sum Sq	Mean Sq	F value	Pr(>F)	
MyoF_T2	2	145.5	72.73	2.739	0.105	
Residuals	12	318.7	26.56			
	Df	Sum Sq	Mean Sq	F value	Pr(>F)	
Cho2	2	169.3	84.63	2.754	0.104	
Residuals	12	368.7	30.73			
	Df	Sum Sq	Mean Sq	F value	Pr(>F)	
MyoF_P	2	425.9	213.0	3.988	**0.047**	*
Residuals	12	640.8	53.4			
	Df	Sum Sq	Mean Sq	F value	Pr(>F)	
Mes3	2	61.31	30.66	2.503	0.123	
Residuals	12	146.99	12.25			
	Df	Sum Sq	Mean Sq	F value	Pr(>F)	
Mes4	2	22.8	11.40	1.045	0.382	
Residuals	12	130.9	10.91			
	Df	Sum Sq	Mean Sq	F value	Pr(>F)	
Cho3	2	90.6	45.30	4.242	**0.0404**	*
Residuals	12	128.1	10.68			

Table S7. The gene symbols for 3 sets of genes whose mRNAs were used for calculation of the module scores shown in Figure 4C. (i) The MyoF_T1 mRNAs were derived from the intersection of the differentially expressed marker genes for MyoF_T1 versus Mes2 clusters. (ii) The MyoF_P mRNAs were derived from the intersection of differentially expressed marker genes for MyoF_P vs Mes2 clusters. (iii) The Mes2 mRNAs were derived from the intersection of the differentially expressed marker genes for Mes2 vs MyoF_T1 clusters.

	MyoF_T1			MyoF_P			Mes2
1	OGN		1	PTGDS		1	TM4SF1
2	LTBP2		2	LIFR		2	NPR3.00
3	LTBP1		3	OGN		3	TXNIP
4	IGFBP7		4	GPNMB		4	EPAS1
5	MMP2		5	LGALS3BP		5	ARHGAP29
6	DPYSL3		6	PLTP		6	INPP4B
7	ITGA1		7	THY1		7	MEF2C
8	COL4A2		8	MATN2		8	FRZB
9	COL4A1		9	ITGA1		9	ALDH1A1
10	GSN		10	LTBP1		10	RERG
11	IGFBP4		11	COL4A1		11	SYTL2
12	SERPINE2		12	COL4A2		12	PLA2G5
13	COL6A3		13	TIMP1		13	ANGPT1
14	TIMP1		14	SPARC		14	ARHGAP15
15	VCAN		15	VCAN		15	EBF1
16	COL1A2		16	FN1		16	NRP1
17	COL1A1		17	HGF		17	AKAP12
18	FN1		18	FBLN5		18	SLC40A1
19	BGN		19	GPC3		19	RAPGEF5
20	THY1		20	IGFBP3		20	EZR
21	FMOD		21	MGP		21	SLC2A3
22	PRSS23		22	PLXDC2		22	APOA2
23	SERPINA1		23	COL6A3		23	NFASC
24	CYP1B1		24	EDNRB		24	PDE1A
25	IGFBP6		25	DPT		25	ALB
26	ELN		26	PDGFRA		26	HMGB2

27	PDGFRA		27	IGFBP7		27	APOA1
28	SPARC		28	LMCD1		28	ZBTB16
29	F3		29	C7		29	HDAC2
30	PDLIM3		30	KRT18		30	DNAJC15
31	FBLN5		31	SERPINA1		31	NHSL2
32	ECM1		32	NR2F1			
33	DPT		33	MASP1			
34	FAP		34	FMOD			
35	S100A6		35	NR2F1-AS1			
36	NR2F1		36	MFAP4			
37	MFAP4		37	PLPP3			
38	ITGBL1		38	MIR99AHG			
39	SPON2		39	C3			
40	C3		40	RAPGEF5			
41	LMCD1		41	FGF7			
42	THBS1		42	PTN			
43	KRT18		43	IL6ST			
44	PRELP		44	MMP2			
45	A2M		45	PCDH9			
46	HSPB6		46	FAP			
47	CFH		47	THBS2			
48	SOD2		48	GPC6			
49	THBS2		49	S100A6			
50	PLTP		50	NRP1			
51	IFI6		51	COL1A2			
52	NR2F1-AS1		52	IGFBP6			
53	EMP1		53	PTGIS			
			54	SPON2			
			55	DPYSL3			
			56	HSPB6			
			57	ABCA8			

			58	SERPINE2			
			59	ARHGAP15			
			60	EMP1			
			61	F3			
			62	APOA2			
			63	PDLIM3			
			64	DNAJC15			
			65	APOA1			
			66	VCAM1			
			67	CFH			
			68	CYP1B1			
			69	THBS1			
			70	ITGBL1			
			71	ANK3			
			72	PRSS23			
			73	LTBP2			
			74	LAMA2			
			75	ELN			
			76	CFI			
			77	SOD2			
			78	CD44			
			79	BGN			
			80	DCN			
			81	COLEC10			
			82	PRELP			
			83	IGFBP4			
			84	A2M			

Table S8. One-way ANOVA and Tukey test for multiple comparisons of the module scores shown in Figure 4C. (**A**) The gene signatures for each cluster (Mes2, MyoF_T1, MyoF_P) were compared with four groups of human liver cells: vascular smooth muscle cells (VSMC); HSC; myofibroblasts; and mesothelia (Meso). The mean module score (Mean) and ratio of module score for each cell type relative to that with the highest mean (Fold) are shown. (**B, C**) Pairwise comparisons between HSC and three other types of human liver cells (VSMC, MyoF and Meso) produce significantly different results ($P<1\times10^{-10}$); and pairwise comparisons between MyoF and the three other types of human liver cells (VSMC, HSC and Meso) also produce significantly different results ($P<1\times10^{-10}$). Taken together, the ANOVA and pairwise comparison results indicate that the gene signature of myofibroblasts in liver is most similar to MyoF_T1 and MyoF_P in microHOs, and that the gene signature of HSC is most similar to Mes2.

Table S8A. The Mean of four liver cell types and different clusters and their relative Fold.

Cluster:	**Mes2**		**MyoF_T1**		**MyoF_P**	
Cell types	**Mean**	**Fold**	**Mean**	**Fold**	**Mean**	**Fold**
VSMC	0.12	2.49	0.18	5.11	0.11	6.86
HSC	**0.31**	1.00	0.32	2.91	0.25	3.09
MyoF	0.06	4.80	**0.92**	1.00	**0.78**	1.00
Meso	-0.07	-4.48	0.49	1.89	0.39	2.00

Table S8B. One-way ANOVA analysis for the four cell types in different clusters.

Cluster	**Source of Variation**	**Sum of Squares**	**Degrees of Freedom**	**Mean Square**	***F*-Calculated**	***P*-Value**
Mes2	Cell Types	28.54	3	9.51	371	$<2\times10^{-16}$
	Residuals	59.03	2299	0.026		
MyoF_T1	Cell Types	137.27	3	45.76	2834	$<2\times10^{-16}$
	Residuals	37.12	2299	0.02		
MyoF_P	Cell Types	110.5	3	36.83	3850	$<2\times10^{-16}$
	Residuals	22	2299	0.01		

Table S8C. Tukey test for multiple comparisons of the module scores.

Cluster	**Pairwise Comparison**	**Mean Difference**	***P*-adjusted**	**95% Confidence Interval**	
				Lower Bound	**Upper Bound**
Mes2	HSC *vs* VSMC	0.19	$<1\times10^{-10}$	0.17	0.20
	MyoF *vs* HSC	-0.24	$<1\times10^{-10}$	-0.27	-0.22
	Meso *vs* HSC	-0.38	$<1\times10^{-10}$	-0.42	-0.34
MyoF_T1	MyoF *vs* VSMC	0.74	$<1\times10^{-10}$	0.72	0.76
	MyoF *vs* HSC	0.61	$<1\times10^{-10}$	0.59	0.62
	Meso *vs* MyoF	-0.44	$<1\times10^{-10}$	-0.47	-0.34
MyoF_P	HSC *vs* VSMC	0.67	$<1\times10^{-10}$	0.65	0.69
	MyoF *vs* HSC	0.53	$<1\times10^{-10}$	0.51	0.55
	Meso *vs* HSC	-0.39	$<1\times10^{-10}$	-0.41	-0.36

Table S9. Summary of the GSEA results assessing the correlation between the MyoF_T1 and MyoF_P gene signatures with NASH **(A**) or hepatocellular carcinoma-associated (HCC) **(B**) non-fibrotic and fibrotic liver tissues. Genes whose expression levels were increased in MyoF_T1 (n=527) or MyoF_P (n=1716) relative to Mes2 were used to form myofibroblast-specific gene expression signatures. The expression data was obtained from (A) early (non-fibrotic) stage 1 and late (fibrotic) stage 4 NASH liver tissue (GSE13525 [2]) or (B) from resected HCC liver tissue, which was classified by pathologists as fibrotic or non-fibrotic (GSE6764 [8]). GSEA analyses revealed that the MyoF_T1 signature was strongly associated with stage 4 NASH, but not with early stage 1 NASH liver tissue; and with liver fibrosis caused by HCC, but not with non-fibrotic HCC liver tissue. The MyoF_P signature had positive associations with stage 4 NASH and HCC-induced fibrotic liver tissue, but those associations were not statistically significant. The expression score (ES), normalized expression score (NES), nominal p-value, and false discovery rate (FDR q-value) are shown for each comparison.

A. NASH Analyses (GSE135251)

Comparison: Stage 4 (Fibrosis)

	ES	NES	P-value	FDR q-value
MyoF_T1	0.56	1.56	0.007	0.018
MyoF_P	0.45	1.32	0.10	0.15

Comparison: Stage 1 (No Fibrosis)

	ES	NES	P-value	FDR q-value
MyoF_T1	-0.30	-0.85	0.66	1
MyoF_P	-0.29	-0.82	0.72	0.87

B. HCC Analyses (GSE6764)

Comparison: Fibrotic Liver

	ES	NES	P-value	FDR q-value
MyoF_T1	0.51	1.71	0.0019	0.05
MyoF_P	0.36	1.48	0.03	0.06

Comparison: Non-fibrotic liver

	ES	NES	P-value	FDR q-value
MyoF_T1	-0.36	-1.32	0.10	0.16
MyoF_P	-0.34	-1.34	0.05	0.22

Table S10. The results of 2-way ANOVA analyses of the data shown in the indicated figures are shown. For these analyses, time and treatment group was treated as categorical variables. The degrees of freedom (DF), the sum of the squares (Sum Sq) and mean squared (mean Sq) of the variance, calculated F-value, and the probability (Pr(>F) from the 2-way ANOVA are shown for the treatment group, time, and treatment-by-time analyses. A Pr(>F) < 0.01 indicates that there was a significant effect of the indicated variable.

Figure 2D	**DF**	**Sum Sq**	**Mean Sq**	**F value**	**Pr(>F)**
Treatment	3	6.11E+14	2.04E+14	110.79	<2.00E-16
Time	4	1.47E+16	3.67E+14	19.98	4.92E-13
Treatment by Time	12	2.48E+14	2.07E+13	11.23	1.66E-15
Residuals	140	2.57E+14	1.84E+12		

Figure 3A	**Df**	**Sum Sq**	**Mean Sq**	**F value**	**Pr(>F)**
Treatment	6	2.96E+14	4.93E+13	14.087	1.24E-12
Time	2	1.08E+15	5.38E+14	153.846	<2.00E-16
Treatment by Time	12	1.44E+14	1.20E+13	3.431	0.000185
Residuals	147	5.14E+14	3.50E+12		

Figure 3B	**Df**	**Sum Sq**	**Mean Sq**	**F value**	**Pr(>F)**
Treatment	5	1.15E+14	2.30E+13	13.919	1.63E-10
Time	2	7.34E+14	3.67E+14	222.459	<2.00E-16
Treatment by Time	10	7.65E+13	7.65E+12	4.637	1.69E-05
Residuals	109	1.80E+14	1.65E+12		

Figure 5B	**Df**	**Sum Sq**	**Mean Sq**	**F value**	**Pr(>F)**
Treatment	3	1.22E+17	4.06E+16	75.096	<2.00E-16
Time	4	2.54E+16	6.36E+15	11.75	2.95E-08
Treatment by Time	12	5.57E+16	4.64E+15	8.578	4.56E-12
Residuals	140	7.57E+16	5.41E+14		

Figure 5C	**Df**	**Sum Sq**	**Mean Sq**	**F value**	**Pr(>F)**
Treatment	3	1.06E+15	3.52E+14	54.89	<2.00E-16
Time	2	5.33E+14	2.66E+14	41.51	1.02E-12
Treatment by Time	6	6.49E+14	1.08E+14	16.86	4.78E-12
Residuals	72	4.62E+14	6.42E+12		

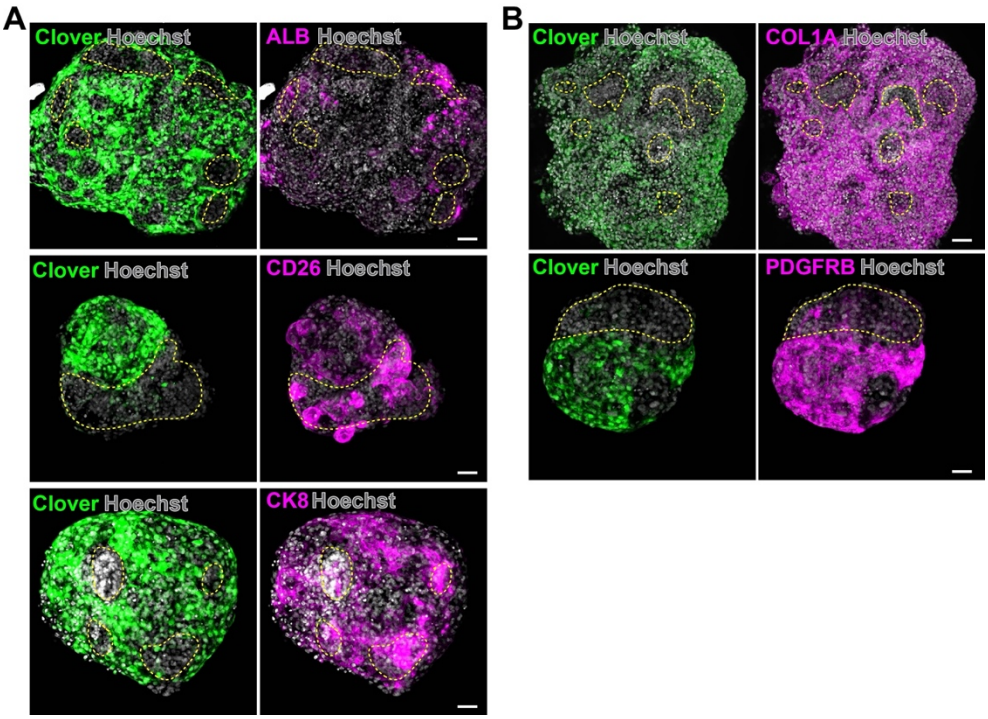

Figure S1. Immunofluorescent images of day 20 *COL1A1*-P2A Clover HOs stained with antibodies to Clover, Albumin (Alb), CD26 and CK8 (**A**); or antibodies to Clover, COL1A and PDGFRB (**B**). As seen in the merged images, the Clover$^+$ cells are distinct from the ALB$^+$ and CD26$^+$ and/or CK8$^+$ hepatocytes and cholangiocytes; while PDGFRB and COL1A are co-expressed in the Clover$^+$ cells. The dotted lines surround areas that are not stained with Clover and the Hoechst staining identifies nuclei. Scale bars, 50 μm.

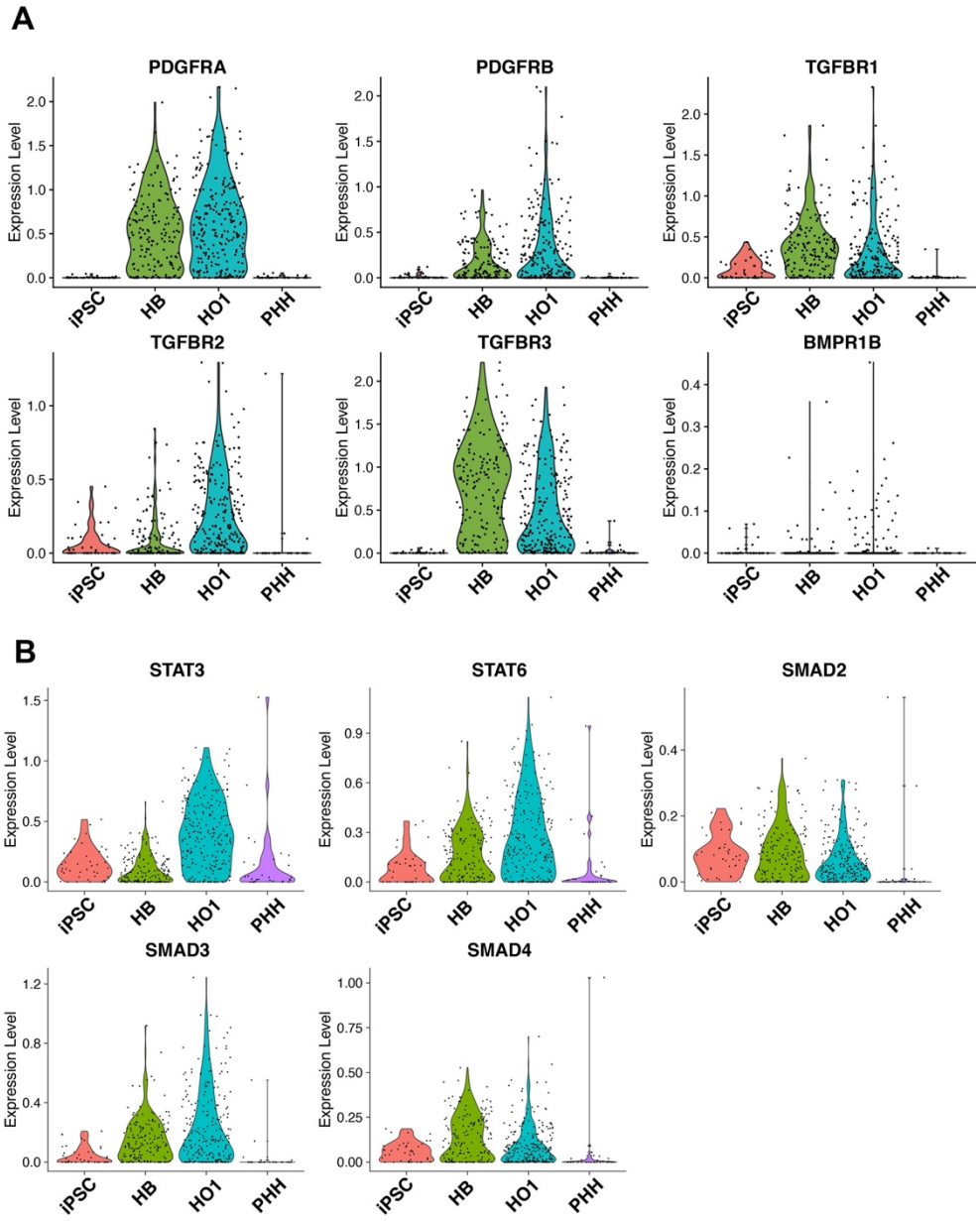

Figure S2. (**A, B**) Violin plots showing the level of expression of mRNAs encoding the receptors for PDGF (*PDGFRA, PDGFRB*) and TGFβ1 (*TGFBR1, TGFBR2, TGFBR3, BMPR1B*); and of *STAT3*, *STAT6*, and *SMAD2-4* mRNAs in developing and mature HO cultures. Previously obtained scRNA-Seq data [24] was generated from iPSC (day 0), day 9 hepatoblast (HB) and day 21 mature organoid cultures. For comparison purposes, scRNA-Seq data obtained from primary human hepatocytes (PHH) is also shown.

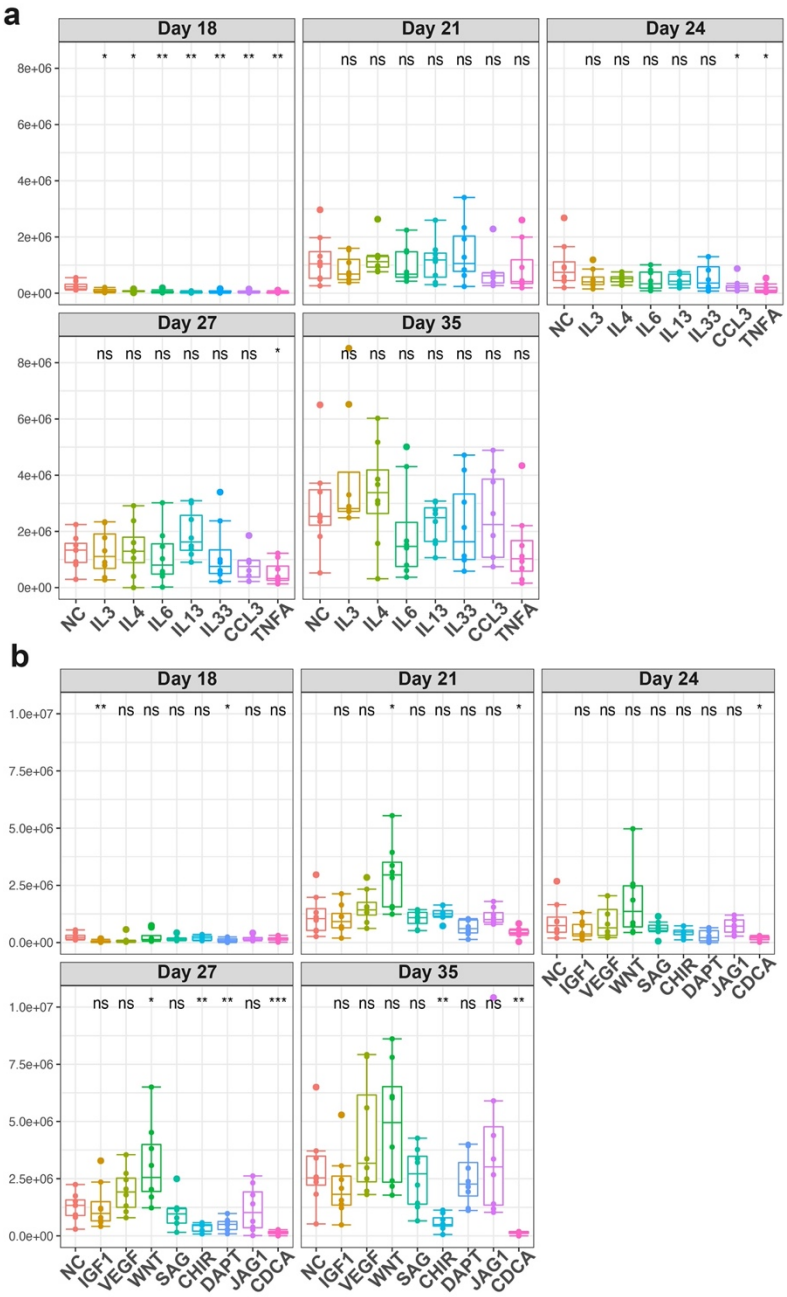

Figure S3. *COL1A1*-P2A Clover HOs were incubated with (**A**) 100 ng/ml IL-3, 100 ng/ml IL-4, 100 ng/ml IL-6, 100 ng/ml IL13, 100 ng/ml IL-33, 100 ng/ml CCL3, 50 ng/ml TNFa; or (**B**) 100 ng/ml IGF1, 50 ng/ml VEGF, 100 ng/ml Wnt3a, 10 μM SAG (Smoothened agonist), 3 μM CHIR99021, 10 μM DAPT (Gamma-Secretase Inhibitor), 100 ng/ml JAG1, 10 μM chenodeoxycholic acid (CDCA), or no addition (NC). Culture fluorescence, which indicates the amount of COL1A1^{+} cells in the HOs, was serially measured on days 18 through 35. Each dot

represents a measurement made on one HO, the thick line is the median of 8 organoids analyzed per condition, and the box plot shows the 25 to 75% range for all measurements per condition. With the possible exception of Wnt3a, none of these added agent caused a significant and or a sustained increase in $COL1A1^+$ cells in any of the organoid cultures. CDCA induced a decrease in $COL1A1^+$ cells.

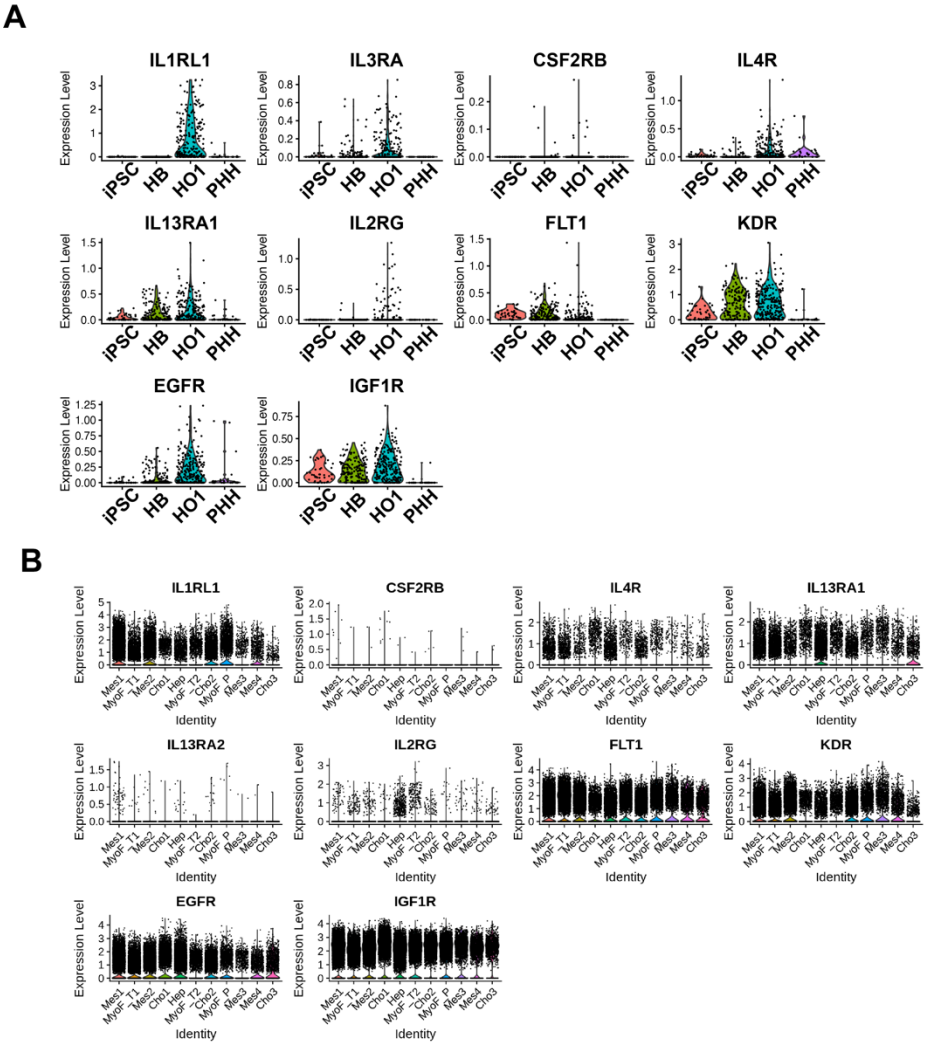

Figure S4. (**A**) Violin plots showing the level of expression of mRNAs for the following receptors during HO development: *IL1RL1, IL4R, IL13RA1, IL2RG, FLT1, KDR,* and *IGF1R*. scRNA-Seq data was generated from iPSC (day 0), day 9 hepatoblast (HB) and day 21 mature organoid (HO1) cultures. For comparison purposes, scRNA-Seq obtained from primary human hepatocytes (PHH) is also shown. This scRNA-Seq dataset was obtained from [24]. (**B**) Violin plots showing the level of mRNA expression for the receptors shown in (A) in the 11 cell clusters identified in day 21 control, PDGF- and TGFβ-treated microHOs using the scRNA-Seq data generated in this paper.

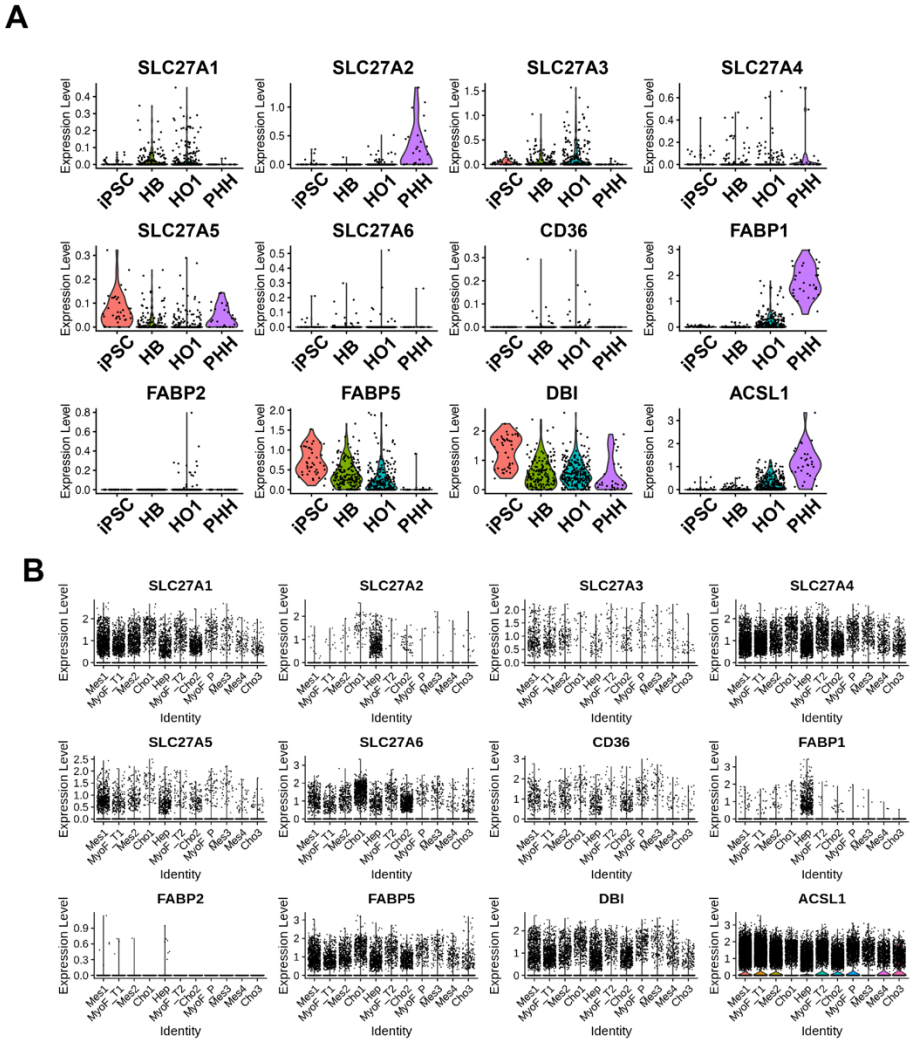

Figure S5. (**A**) Violin plots showing the level of expression of mRNAs for the following fatty acid transport proteins during HO development: *SLC27A1-6, CD36, FABP1-2, FABP5, DBI* and *ACSLI.* The previously obtained scRNA-Seq data [24] was generated from iPSC (day 0), day 9 hepatoblast (HB) and day 21 mature organoid cultures. For comparison purposes, scRNA-Seq obtained from primary human hepatocytes (PHH) is also shown. (**B**) Violin plots showing the level of mRNA expression for the for the fatty acid transport proteins shown in (A) in the eleven cell clusters identified in day 21 control, PDGF- and TGFβ-treated microHOs using the scRNA-Seq data generated in this paper.

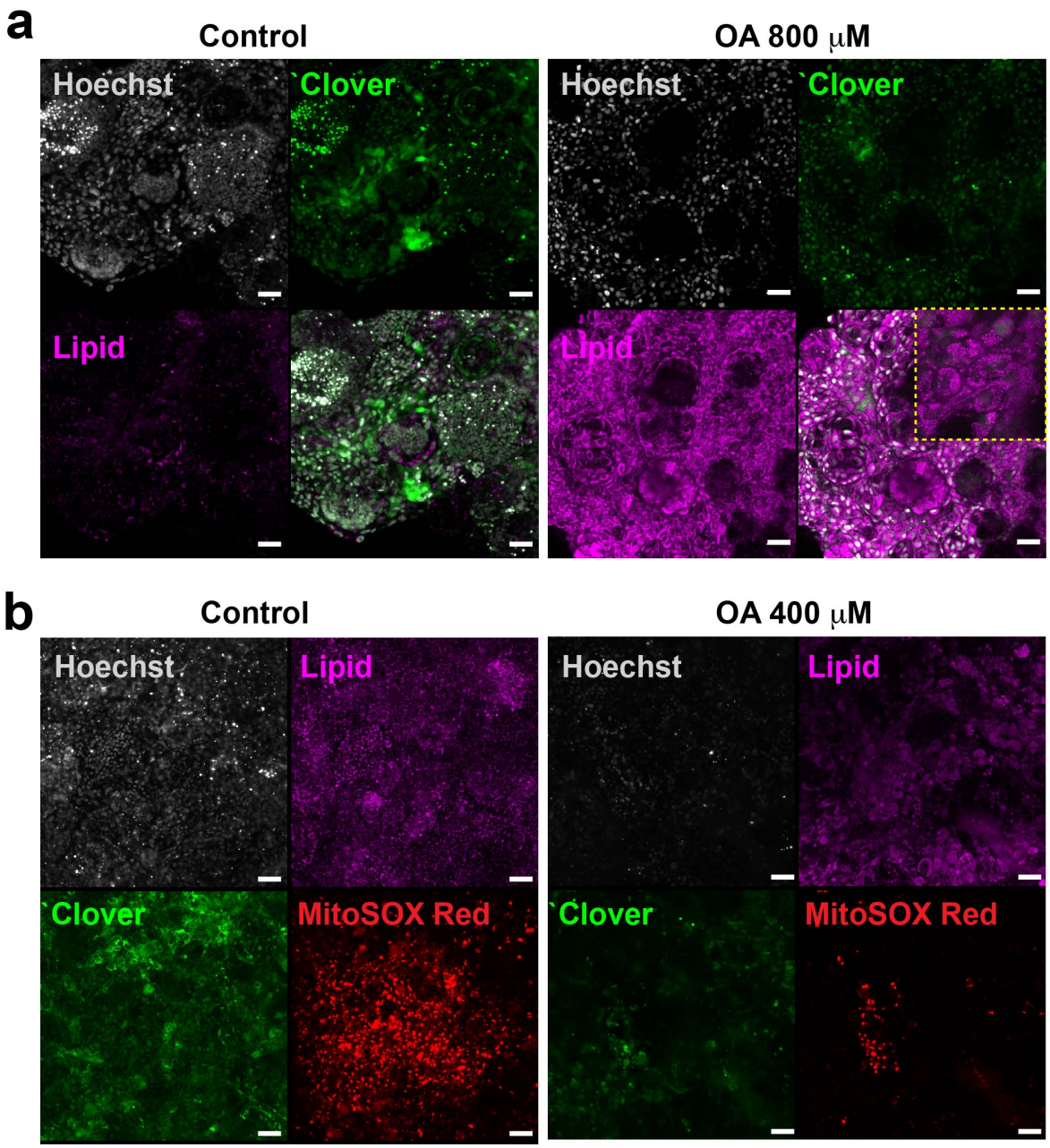

Figure S6. Oleic acid (OA) induces toxicity in HOs. Either 800 (**A**) or 400 (**B**) uM OA was added to HO cultures on day 13, and the HOs were analyzed by the HCS system on day 24. Although there was a marked increase in intracellular fatty acids within the HOs that were incubated with OA (LipidSpot), OA addition did not increase in COL1A1 expression (Clover). Moreover, there was a marked decrease in cell viability within the HOs that were incubated with OA, as shown by the MitoSox Red analysis.

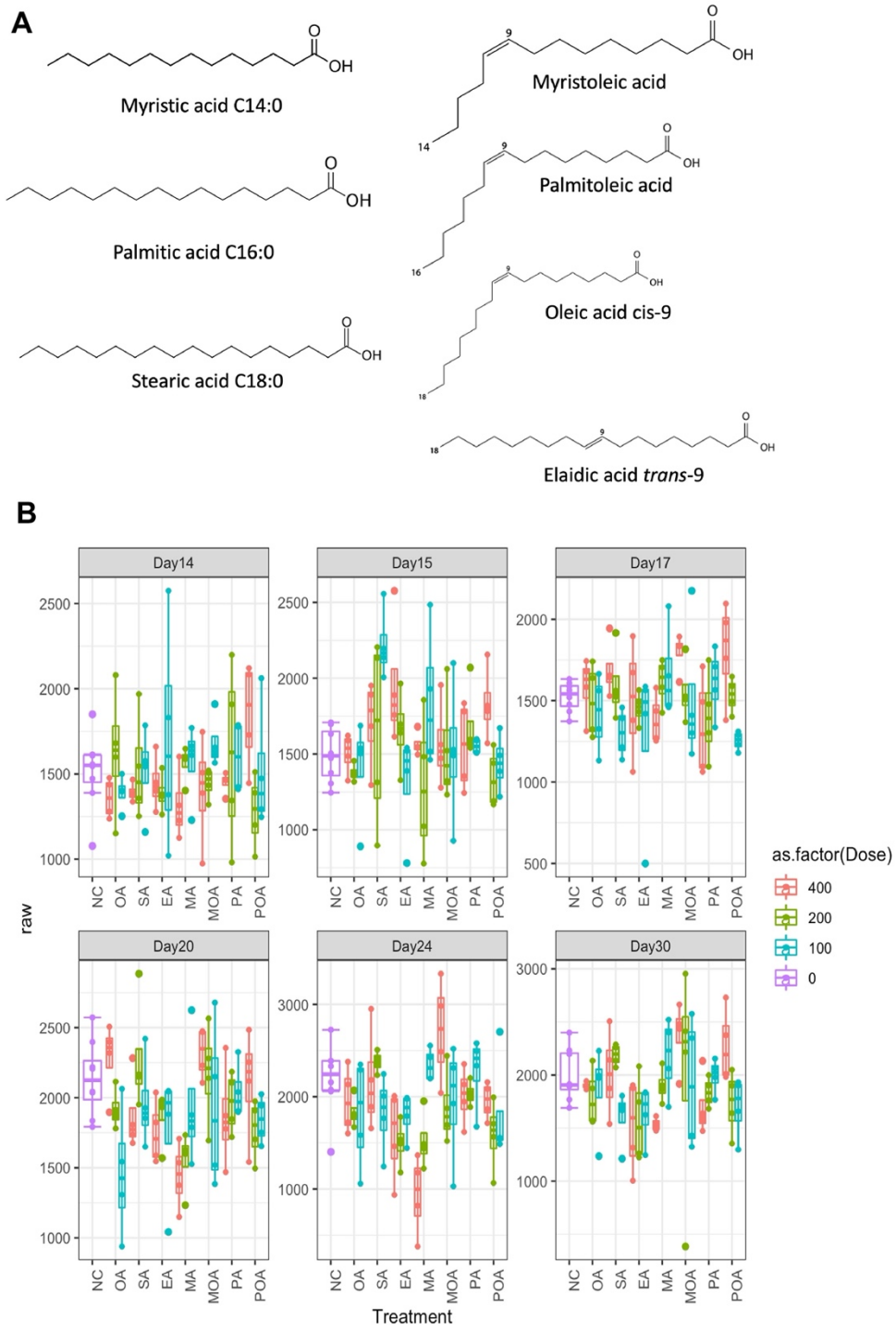

Figure S7. Free fatty acids do not increase collagen expression in HOs. (**A**) The structures of the free fatty acids whose effect on collagen expression in HOs was analyzed. Unsaturated FFAs (myristic (MA), palmitic (PA) and stearic (SA)) and their corresponding FFA with cis-9 (Myristoleic (MOA), palmitoleic (POA), and oleic (OA)) or trans-9 (elaidic (EA)) double bonds were analyzed. (**B**) *COL1A1*-P2A Clover HOs were incubated with 0, 100, 200 or 400 uM of the

indicated free fatty acid on day 13. The fluorescence in these cultures, which indicates the amount of COL1A1^{+} cells in the HOs, was serially measured on days 14 through 30. Each dot represents a measurement made on one HO, the thick line is the median of 8 organoids analyzed per condition, and the box plot shows the 25 to 75% range for all measurements per condition. The free fatty acids did not induce a significant increase in COL1A1^{+} in any of the cultures.

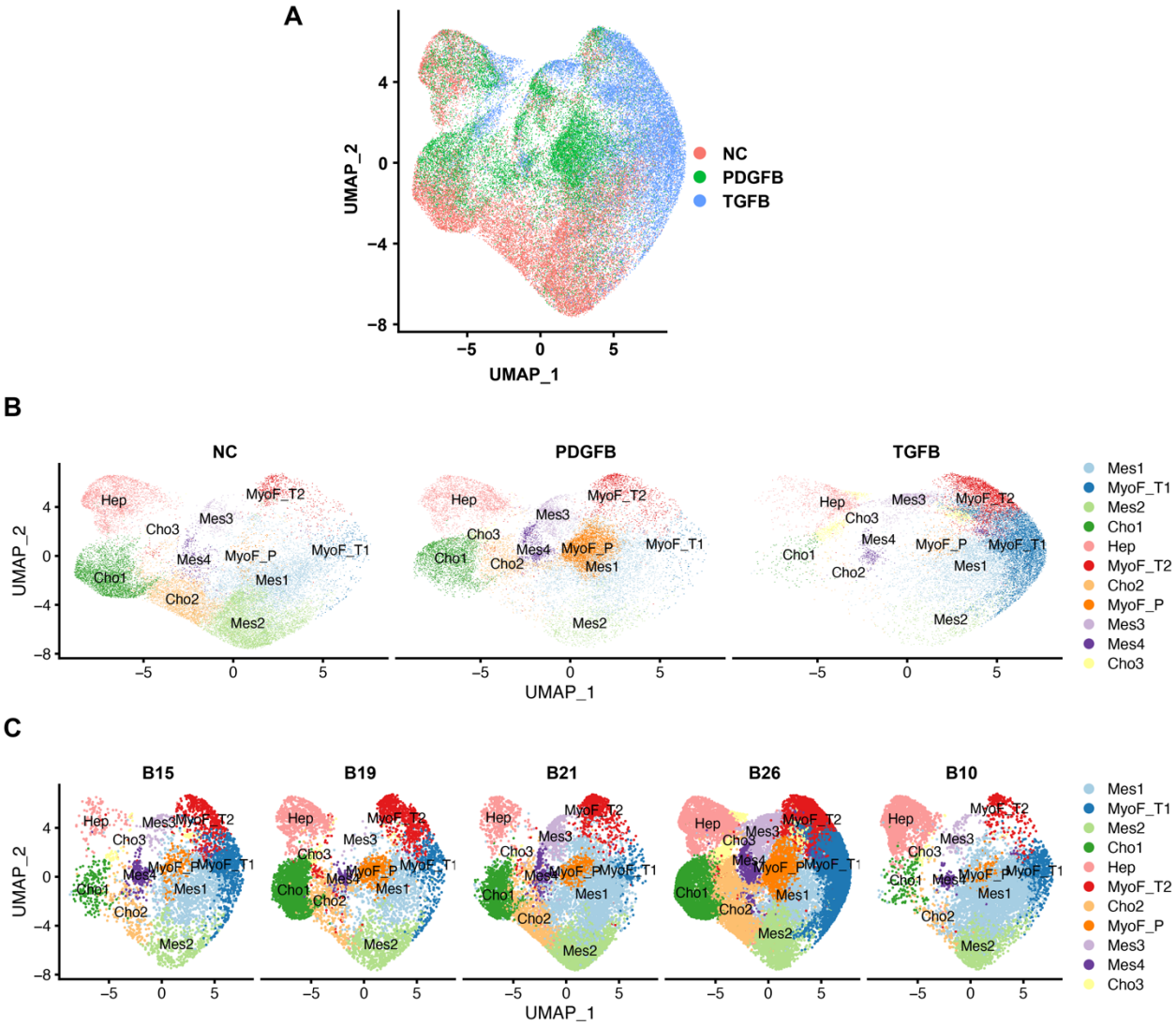

Figure S8. (**A**) A combined sample u-MAP plot shows the scRNA-seq data obtained from the cells in day 21 control (NC), PDGFβ-, or TGFβ1-treated microHO cultures. Each of the different type of microHO is indicated by the color shown on the right of the panel. (**B**) Separate u-MAP plots show the scRNA-seq data obtained from the cells in day 21 control (NC), PDGFβ-, or TGFβ1-treated microHO cultures. (**C**) The u-MAP plots for each of the five batches of microHOs that were separately analyzed by scRNA-Seq analysis. Each cluster is indicated by a different color as indicated on the right side of panels B and C.

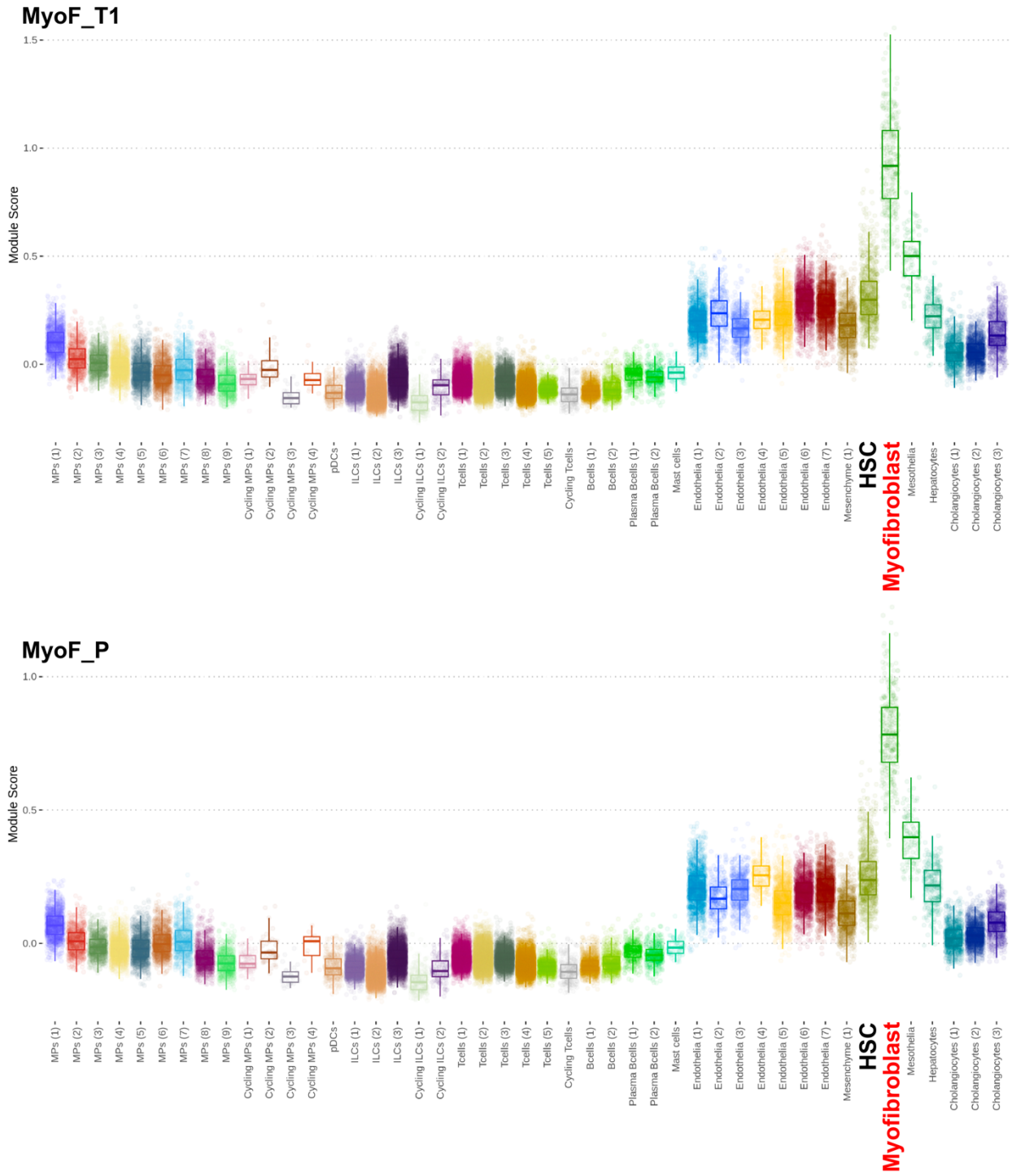

Figure S9. Among the multiple different types of cells present in normal and cirrhotic human liver, the MyoF_T1 and MyoF_P transcriptomes are most like that of myofibroblasts. The MyoF_T1 (n=53 genes) or MyoF_P (n=84 genes) signatures were compared with the transcriptomes of the various cell types in normal and cirrhotic human liver tissue (GSE136103 [21]), which include macrophages (MP) and innate lymphoid cells (ILC).). Each dot shows the modulus score obtained when the gene signatures for the cell type indicated on the x-axis was compared with that of MyoF_T1 or MyoF_P. The thick line shows the mean, the boxplots show the 25 to 75% range, and the vertical line shows the Minimum (Q0 or 0th percentile) and

Maximum (Q4 or 100th percentile) of the scores. The MyoF_T1 and MyoF_P signatures are most enriched in the myofibroblasts in human liver tissue. The dotted lines represent actual reference module scores.

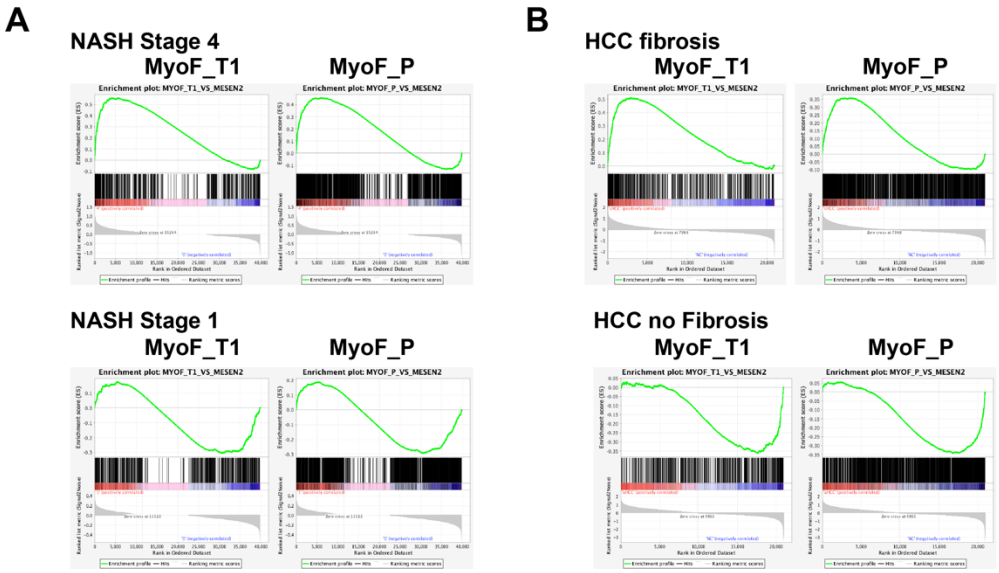

Figure S10. GSEA results assessing the correlation between the MyoF_T1 and MyoF_P gene signatures with that of non-fibrotic and fibrotic liver tissues caused by NASH **(A**) or hepatocellular carcinoma (HCC) **(B**). Genes whose expression levels were increased in MyoF_T1 (n=527) or MyoF_P (n=1716) relative to Mes2 (**Table S*)** were used to form myofibroblast-specific gene expression signatures. GSEA was performed using expression data obtained from (A) early (non-fibrotic) stage 1 and late (fibrotic) stage 4 NASH liver tissue (GSE13525 [2]) or (B) from resected HCC liver tissue, which was classified by histologic analysis as fibrotic or non-fibrotic (GSE6764 [8]). GSEA analyses revealed that the MyoF_T1 (NSE 1.7; false discovery rate (FDR) 3.3×10^{-4}) and MyoF_P (1.4; FDR 0.013) signatures were strongly associated with stage 4 NASH liver tissue, but not with early (NES -0.97 and -0.95, FDR 1 and 0.99, respectively) stage 1 NASH liver tissue; and the MyoF_T1 (NES 2.77, FDR 0) and MyoF_P (NES 1.8, FDR 4.4×10^{-4}) signatures were associated with liver fibrosis caused by HCC, whereas the MyoF_T1 (NES -1.98, FDR 0) and MyoF_P (NES -1.97, FDR 0) signatures were not associated with non-fibrotic HCC liver tissue.

HNF4A
Clover
HNF4A_Clover
SERPINA1
Clover
SERPINA1_Clover
CDH1
Clover
CDH1_Clover
AFP
Clover
AFP_Clover
KRT19
Clover
KRT19_Clover
KRT7
Clover
KRT7_Clover
rna_SOX9
Clover
rna_SOX9_Clover
CFTR
Clover
CFTR_Clover
ALDH1A1
Clover
ALDH1A1_Clover
APOB
Clover
APOB_Clover
FGB
Clover
FGB_Clover
NC
PDGFB
TGFB

Figure S11. Feature plots show the level of expression of each indicated mRNA with *Clover* mRNA in the u-MAP plots shown in Fig 8B. The uMAP plots for the normal control (NC), PDGF-, and TGFβ-treated microHOs are shown separately. The colors represent level of expression of the two mRNAs in each row as shown in the adjacent color threshold diagram. The mRNAs found in cholangiocytes (*KRT19*, *KRT7*, *CFTR),* hepatocytes *(SERPIN1A)* or hepatocytes and cholangiocytes (*HNF4A, AFP, CDH1, ALDHA1, APOB, SOX9, FGB*) were not expressed in the cells that expressed *Clover* mRNA in the microHOs.

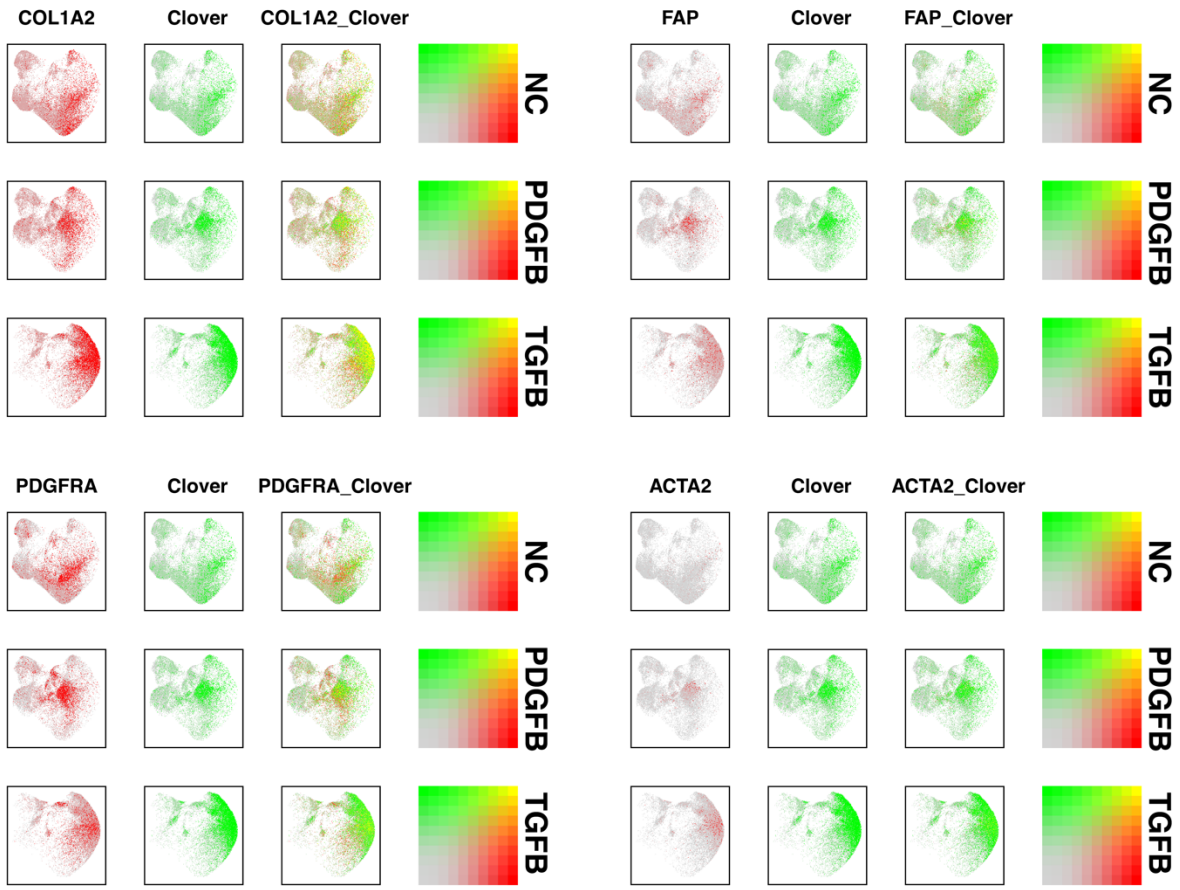

Figure S12. Feature plots show the level of expression of *COL1A2, PDGFRA, FAP or ACTA2* mRNAs with *Clover* mRNA in the u-MAP plots shown in Fig 8B. The u-MAP plots for the normal control (NC), PDGF-, and TGFβ-treated microHOs are shown separately. The colors represent level of expression of the two mRNAs in each row as shown in the adjacent color threshold diagram. *COL1A2 and Clover* mRNAs have an overlapping pattern of expression; they are expressed in myofibroblasts and in mesenchymal cells. In contrast, *ACTA2, PDGFRA* and *FAP* mRNAs are predominantly expressed in the myofibroblasts (MyoF-T1/2, MyoF_P) in PDGF- or TGFβ-treated microHOs.

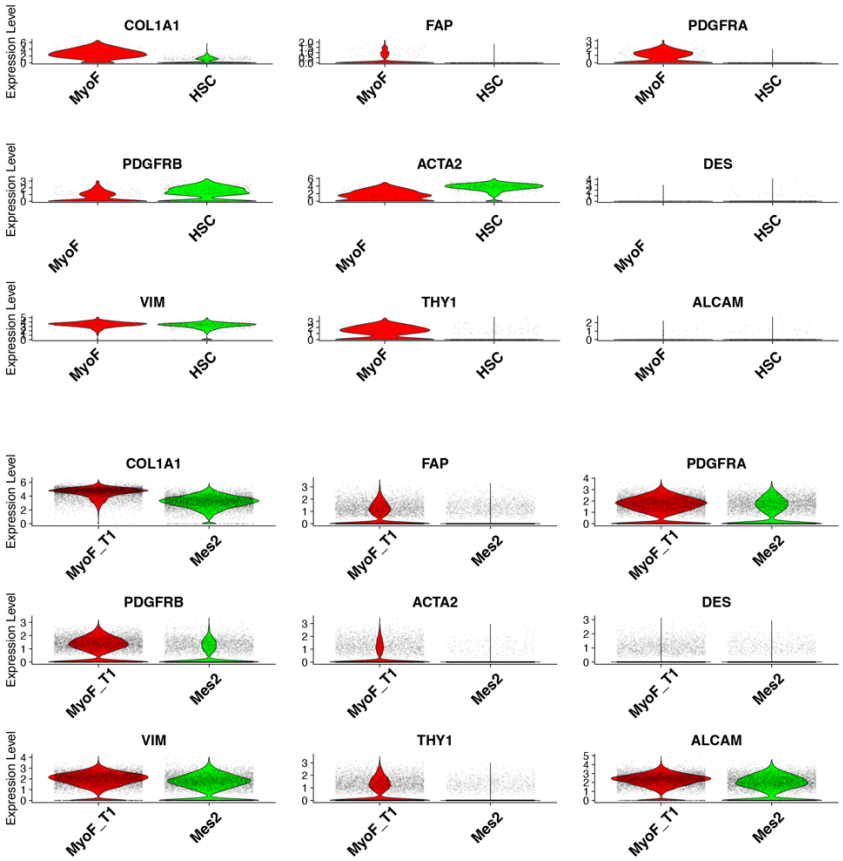

Figure S13. The pattern of expression of mesenchyme and MyoF-specific genes in hepatic stellate cells (HSC) and MyoF in human liver is mostly retained in Mes2 and MyoF_T1 cells in microHOs. scRNA-Seq data was analyzed to generate violin plots showing the level of expression of *COL1A1, FAP, PDGFRA, PDGFRB, ACTA2, DES, VIM, Thy1* and *ALCAM* mRNAs in HSC and MyoF in cirrhotic human liver (GSE136103; Top panel) and in Mes2 and MyoF_T1 cells in microHOs (Bottom panel). The cell cluster is indicated on the x-axis; and the y-axis shows the natural log transformed and normalized level of expression of each mRNA. Each dot shows the expression level in one cell.

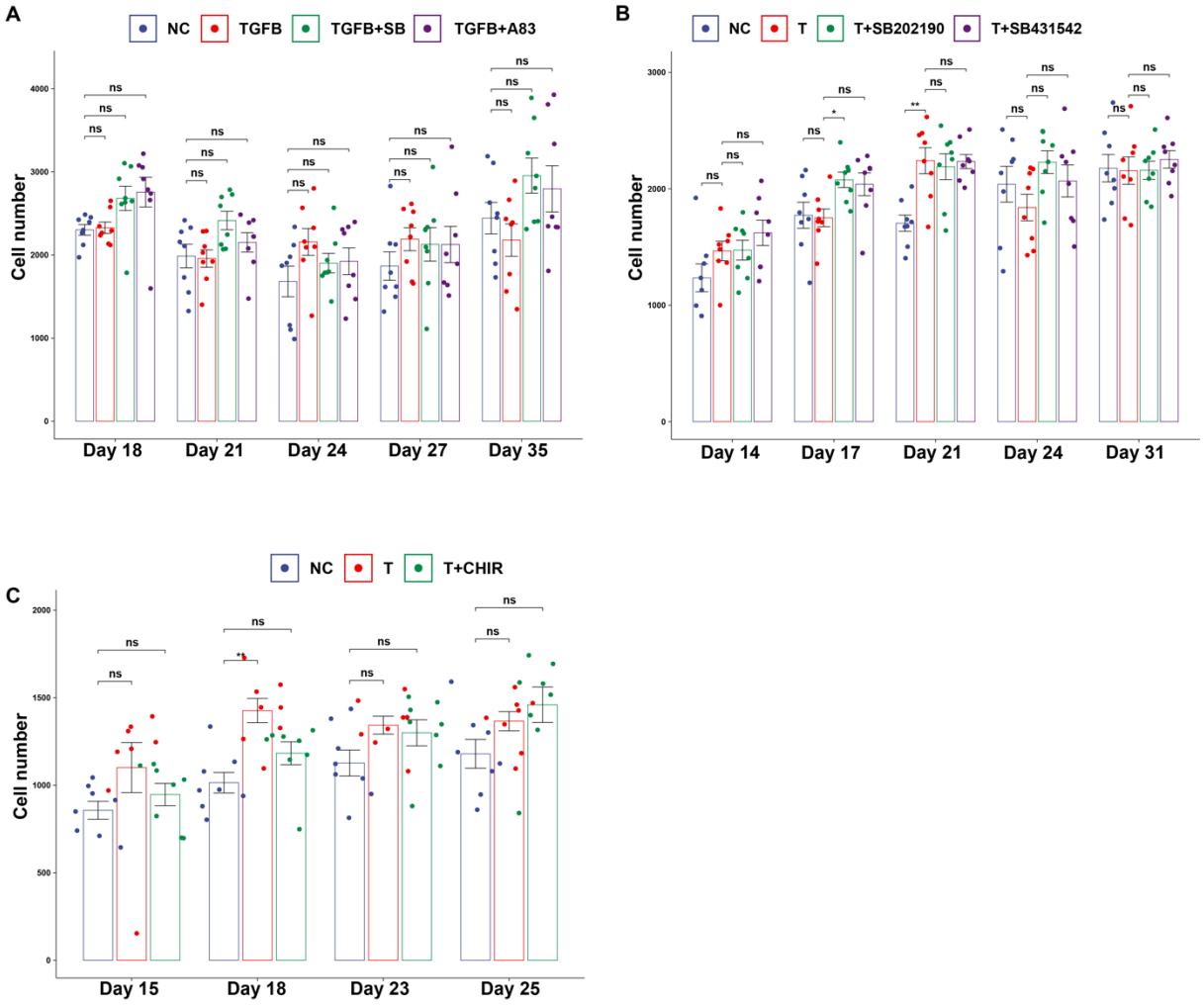

Figure S14. microHO viability was not affected by addition of TGFβ1, nor by any of the other tested drugs. microHOs were prepared and incubated with no addition (NC), 50 ng/ml TGFβ1 (T), or TGFβ1 ± the indicated inhibitor on day 13. The tested drugs were: (**A)** 10 uM TGFRβ1 tyrosine kinase inhibitors A83-01 or SB431542 (SB); (**B**) 10 uM TGFRβ1 inhibitor (SB431542) or 10 uM p38 α inhibitor (SB202190); and (**C**) 10 uM CHIR99021 (CHIR). The number of cells in each microHO was measured by counting the number of nuclei (stained with Hoechst 33342) on days 14 to 35. Each bar is the average of 8 individual measurements ± the SE, and individual datapoints are shown as dots. None of these additions caused a significant change (ns) in the number of cells in the treated microHOs relative to control microHOs.

Table S5. Twenty mRNAs that are differentially expressed in each of the 11 cell clusters identified in microHOs. The gene symbol, p-value, adjusted p-value, and fold differential expression (log_2) for each differentially expressed gene are shown. Pct.1 and Pct.2 indicates the contribution of that feature to defining the indicated cluster based upon principal component analysis.

	cluster	gene	p_val	avg_log2FC	pct.1	pct.2	p_val_adj
1	0	*COL14A1*	0.00	0.74	0.77	0.55	0
2	0	*ADAMTS1*	0.00	0.69	0.87	0.6	0
3	0	*KCND2*	0.00	0.65	0.75	0.53	1.41073166685289E-295
4	0	*DLK1*	0.00	0.64	0.97	0.88	0
5	0	*IL1RL1*	0.00	0.63	0.6	0.4	6.07272463504603E-113
6	0	*COL6A3*	0.00	0.58	0.99	0.93	0
7	0	*IL6ST*	0.00	0.57	0.99	0.95	0
8	0	*ITGA1*	0.00	0.56	0.93	0.74	0
9	0	*ZNF804A*	0.00	0.55	0.85	0.66	9.89305658045823E-202
10	0	*CLMP*	0.00	0.55	0.92	0.68	0
11	0	*PDGFRA*	0.00	0.54	0.91	0.76	0
12	0	*SOX5*	0.00	0.54	1	0.99	0
13	0	*DCN*	0.00	0.54	0.98	0.89	0
14	0	*LAMA2*	0.00	0.53	0.96	0.8	0
15	0	*LUM*	0.00	0.51	0.96	0.82	0
16	0	*SERPINE2*	0.00	0.49	0.99	0.93	0
17	0	*DPP4*	0.00	0.49	0.97	0.85	0
18	0	*COL1A2*	0.00	0.48	1	0.99	2.39332526066761E-224
19	0	*RSPO2*	0.00	0.47	0.9	0.69	0
20	0	*TGFBR3*	0.00	0.45	0.88	0.65	0
21	1	*CILP*	0.00	2.11	0.98	0.8	0
22	1	*TIMP3*	0.00	1.99	1	0.96	0
23	1	*COMP*	0.00	1.96	0.87	0.67	0
24	1	*ITGA11*	0.00	1.52	0.88	0.64	0
25	1	*COL1A1*	0.00	1.49	1	0.98	0

26	1	*AC097487.1*	0.00	1.48	0.65	0.59	0
27	1	*TRABD2B*	0.00	1.43	0.9	0.64	0
28	1	*MXRA5*	0.00	1.37	0.96	0.79	0
29	1	*TIMP1*	0.00	1.32	1	0.97	0
30	1	*CCN2*	0.00	1.32	0.86	0.67	0
31	1	*ABTB2*	0.00	1.32	0.98	0.76	0
32	1	*LTBP2*	0.00	1.30	0.91	0.67	0
33	1	*NOX4*	0.00	1.27	0.93	0.76	0
34	1	*EGFP*	0.00	1.27	0.96	0.82	0
35	1	*SMYD3*	0.00	1.27	0.99	0.93	0
36	1	*AF165147.1*	0.00	1.23	0.81	0.71	0
37	1	*SPON1*	0.00	1.22	0.75	0.55	0
38	1	*SERPINE2*	0.00	1.22	1	0.94	0
39	1	*MICAL2*	0.00	1.17	0.96	0.79	0
40	1	*CLU*	0.00	1.17	0.92	0.73	0
41	2	*CNTN5*	0.00	2.15	0.88	0.64	0
42	2	*LINC01088*	0.00	2.05	0.97	0.71	0
43	2	*LINC02388*	0.00	2.05	0.93	0.66	0
44	2	*POSTN*	0.00	1.70	0.95	0.74	0
45	2	*NPNT*	0.00	1.67	0.92	0.73	0
46	2	*ARHGAP6*	0.00	1.63	0.88	0.59	0
47	2	*SLIT3*	0.00	1.58	0.91	0.78	0
48	2	*DIRC3*	0.00	1.48	0.91	0.68	0
49	2	*PKHD1L1*	0.00	1.44	0.76	0.51	0
50	2	*CLSTN2*	0.00	1.35	0.82	0.62	0
51	2	*BCO2*	0.00	1.35	0.94	0.69	0
52	2	*PDPN*	0.00	1.29	0.98	0.87	0
53	2	*CPS1*	0.00	1.28	0.94	0.7	0
54	2	*KCNMA1*	0.00	1.26	0.94	0.8	0
55	2	*LINC00894*	0.00	1.26	0.92	0.68	0
56	2	*PWWP3B*	0.00	1.25	0.87	0.59	0

57	2	*COL11A1*	0.00	1.25	0.98	0.87	0
58	2	*KDR*	0.00	1.24	0.87	0.59	0
59	2	*PRLR*	0.00	1.24	0.96	0.77	0
60	2	*GHR*	0.00	1.23	0.88	0.68	0
61	3	*UNC5C*	0.00	2.45	0.96	0.62	0
62	3	*GRHL2*	0.00	2.36	0.91	0.64	0
63	3	*ITGB6*	0.00	2.32	0.96	0.7	0
64	3	*GABRP*	0.00	2.29	0.86	0.58	0
65	3	*PDE4D*	0.00	2.20	0.96	0.81	0
66	3	*ARHGAP29*	0.00	2.11	0.89	0.51	0
67	3	*PLD5*	0.00	2.08	0.86	0.67	0
68	3	*ROR1*	0.00	2.08	0.86	0.56	0
69	3	*AC015522.1*	0.00	2.00	0.98	0.77	0
70	3	*PRTG*	0.00	1.93	0.83	0.51	0
71	3	*NRXN3*	0.00	1.88	0.89	0.66	0
72	3	*ST6GALNAC3*	0.00	1.85	0.89	0.66	0
73	3	*NEBL*	0.00	1.85	0.91	0.75	0
74	3	*ANKS1A*	0.00	1.81	0.88	0.77	0
75	3	*EYA1*	0.00	1.76	0.67	0.53	0
76	3	*NAALADL2*	0.00	1.75	0.84	0.65	0
77	3	*SEMA5A*	0.00	1.74	0.95	0.73	0
78	3	*PTN*	0.00	1.67	0.8	0.55	0
79	3	*THSD4*	0.00	1.65	0.84	0.56	0
80	3	*PATJ*	0.00	1.64	0.82	0.63	0
81	4	*AFP*	0.00	3.58	0.72	0.53	0
82	4	*CHST9*	0.00	1.90	0.77	0.39	0
83	4	*APOB*	0.00	1.82	0.51	0.46	1.57013013564819E-97
84	4	*CEACAM6*	0.00	1.79	0.65	0.44	0
85	4	*FGB*	0.00	1.71	0.55	0.45	7.57761739439617E-259
86	4	*LINC00511*	0.00	1.68	0.87	0.54	0
87	4	*NTN4*	0.00	1.68	0.71	0.55	0

88	4	*SERPINA1*	0.00	1.58	0.53	0.43	3.26816794412982E-195
89	4	*DNAJC15*	0.00	1.47	0.91	0.73	0
90	4	*CDH17*	0.00	1.44	0.58	0.44	0
91	4	*CDH2*	0.00	1.38	0.95	0.79	0
92	4	*FOXP2*	0.00	1.37	0.73	0.55	0
93	4	*EPCAM*	0.00	1.26	0.75	0.52	0
94	4	*APOA1*	0.00	1.25	0.62	0.37	0
95	4	*MARCHF1*	0.00	1.23	0.64	0.44	0
96	4	*CDH1*	0.00	1.23	0.77	0.55	0
97	4	*CCSER1*	0.00	1.21	0.8	0.54	0
98	4	*MAML3*	0.00	1.20	0.9	0.75	0
99	4	*LINC00278*	0.00	1.20	0.78	0.59	0
100	4	*LCP1*	0.00	1.16	0.76	0.55	0
101	5	*PI16*	0.00	2.48	0.92	0.74	0
102	5	*C3*	0.00	2.00	0.74	0.59	0
103	5	*IGFBP6*	0.00	1.93	0.81	0.67	0
104	5	*HTRA3*	0.00	1.86	0.77	0.63	0
105	5	*GABRB3*	0.00	1.69	0.4	0.47	0.645287107
106	5	*SLC24A2*	0.00	1.49	0.75	0.65	0
107	5	*KRT14*	0.00	1.32	0.65	0.58	0
108	5	*PRSS23*	0.00	1.30	0.83	0.69	0
109	5	*TIMP3*	0.00	1.21	1	0.96	0
110	5	*ATP10A*	0.00	1.19	0.78	0.69	0
111	5	*ANK2*	0.00	1.19	0.85	0.73	0
112	5	*TNS1*	0.00	1.17	0.87	0.73	0
113	5	*CSPG4*	0.00	1.16	0.7	0.59	0
114	5	*CD55*	0.00	1.14	0.72	0.67	4.49192035504069E-284
115	5	*KLF3*	0.00	1.10	0.78	0.71	0
116	5	*CPAMD8*	0.00	1.07	0.58	0.42	0
117	5	*AC099520.1*	0.00	1.05	0.5	0.5	2.92243869181999E-49
118	5	*ABI3BP*	0.00	1.04	0.76	0.67	0

119	5	*ZBTB7C*	0.00	1.03	0.57	0.58	3.96295910582397E-99
120	5	*FLNC*	0.00	1.02	0.73	0.61	0
121	6	*UNC5C*	0.00	0.84	0.94	0.63	0
122	6	*GABRP*	0.00	0.78	0.79	0.6	0
123	6	*ST6GALNAC3*	0.00	0.78	0.9	0.67	0
124	6	*GRHL2*	0.00	0.77	0.89	0.65	0
125	6	*PRTG*	0.00	0.71	0.82	0.53	0
126	6	*PDE4D*	0.00	0.69	0.96	0.82	0
127	6	*ROR1*	0.00	0.69	0.85	0.57	0
128	6	*ARHGAP29*	0.00	0.68	0.83	0.54	0
129	6	*ANKS1A*	0.00	0.65	0.91	0.77	0
130	6	*ITGB6*	0.00	0.65	0.93	0.71	0
131	6	*PLD5*	0.00	0.62	0.84	0.68	0
132	6	*LINC02388*	0.00	0.61	0.74	0.69	3.14703394653217E-146
133	6	*EYA1*	0.00	0.60	0.67	0.54	1.6275168304562E-266
134	6	*DIAPH3*	0.00	0.60	0.68	0.55	1.51594497149573E-217
135	6	*NRXN3*	0.00	0.59	0.88	0.67	0
136	6	*FREM2*	0.00	0.59	0.66	0.52	1.11716953189223E-242
137	6	*KCNQ5*	0.00	0.58	0.73	0.57	5.17999574470969E-237
138	6	*AC015522.1*	0.00	0.58	0.97	0.78	0
139	6	*PTN*	0.00	0.57	0.71	0.57	6.4862311734237E-293
140	6	*SEMA5A*	0.00	0.57	0.94	0.74	0
141	7	*TFPI2*	0.00	2.00	0.62	0.46	0
142	7	*PAPPA*	0.00	1.65	0.98	0.89	0
143	7	*PDE5A*	0.00	1.55	0.73	0.57	0
144	7	*ADAMTS1*	0.00	1.53	0.8	0.65	0
145	7	*AREG*	0.00	1.35	0.69	0.64	5.25882782978605E-270
146	7	*ITGA1*	0.00	1.26	0.88	0.77	0
147	7	*ABCC4*	0.00	1.23	0.71	0.64	0
148	7	*MSC-AS1*	0.00	1.20	0.55	0.51	1.60206265130991E-185
149	7	*PIEZO2*	0.00	1.13	0.62	0.48	3.62254977687614E-291

150	7	*SUCLG2-AS1*	0.00	1.12	0.73	0.65	0
151	7	*CLMP*	0.00	1.11	0.79	0.72	0
152	7	*KYNU*	0.00	1.07	0.45	0.5	1.09972579275846E-41
153	7	*IGFBP5*	0.00	1.06	0.86	0.8	0
154	7	*ROBO2*	0.00	1.05	0.84	0.71	0
155	7	*RORB*	0.00	1.05	0.64	0.65	1.71419981781713E-181
156	7	*MASP1*	0.00	0.98	0.6	0.52	2.14815931343417E-221
157	7	*AL691420.1*	0.00	0.94	0.69	0.74	1.90329965031377E-129
158	7	*KCND2*	0.00	0.94	0.6	0.58	1.12904013826135E-87
159	7	*PAMR1*	0.00	0.93	0.66	0.64	1.05279467805712E-135
160	7	*MMP16*	0.00	0.91	0.79	0.73	6.45407093018707E-251
161	8	*CXCL14*	0.00	2.54	0.82	0.61	0
162	8	*KIRREL3*	0.00	2.47	0.64	0.58	1.78087718527724E-275
163	8	*NRP2*	0.00	2.07	0.81	0.59	0
164	8	*GSN*	0.00	2.01	0.93	0.84	0
165	8	*AC002463.1*	0.00	1.95	0.66	0.56	0
166	8	*CRHBP*	0.00	1.89	0.53	0.52	2.68844774508409E-87
167	8	*ATRNL1*	0.00	1.84	0.67	0.58	7.4046528162926E-205
168	8	*NRG3*	0.00	1.81	0.78	0.51	0
169	8	*CDH13*	0.00	1.79	0.63	0.48	1.90104856701329E-243
170	8	*MIAT*	0.00	1.79	0.7	0.56	0
171	8	*NTM*	0.00	1.77	0.59	0.55	1.11151682293596E-121
172	8	*PLCB4*	0.00	1.76	0.74	0.59	0
173	8	*OXCT1*	0.00	1.76	0.61	0.56	1.22313326537527E-195
174	8	*NPAS2*	0.00	1.59	0.67	0.53	1.64759745644261E-255
175	8	*PI16*	0.00	1.56	0.8	0.76	2.48410109644837E-303
176	8	*CD109*	0.00	1.54	0.75	0.7	3.32247596107369E-263
177	8	*LINC01592*	0.00	1.53	0.54	0.55	4.53240260414655E-120
178	8	*TEK*	0.00	1.48	0.73	0.63	7.56466873318405E-289
179	8	*PARD3B*	0.00	1.45	0.76	0.7	1.08312332593575E-226
180	8	*PODXL*	0.00	1.43	0.76	0.7	2.30063348380999E-244

181	9	*MKI67*	0.00	2.57	0.94	0.59	0
182	9	*TOP2A*	0.00	2.44	0.89	0.56	0
183	9	*CENPF*	0.00	2.23	0.89	0.58	0
184	9	*ASPM*	0.00	2.09	0.86	0.53	0
185	9	*TPX2*	0.00	2.02	0.88	0.57	0
186	9	*CENPE*	0.00	1.62	0.78	0.44	0
187	9	*DIAPH3*	0.00	1.56	0.88	0.55	0
188	9	*ANLN*	0.00	1.56	0.82	0.49	0
189	9	*PRC1*	0.00	1.39	0.73	0.44	0
190	9	*KIF11*	0.00	1.37	0.77	0.49	0
191	9	*NUSAP1*	0.00	1.36	0.71	0.41	0
192	9	*CIT*	0.00	1.34	0.75	0.5	0
193	9	*KPNA2*	0.00	1.31	0.73	0.46	3.90947789658089E-290
194	9	*CDK1*	0.00	1.27	0.68	0.51	1.05324536288692E-221
195	9	*KIF4A*	0.00	1.26	0.71	0.49	0
196	9	*NCAPG*	0.00	1.19	0.7	0.5	6.08843872357421E-298
197	9	*CEP128*	0.00	1.18	0.79	0.55	3.67991367428791E-298
198	9	*KIF14*	0.00	1.17	0.66	0.45	1.75116932862194E-259
199	9	*CKAP2L*	0.00	1.16	0.69	0.51	7.57255848194669E-251
200	9	*MIR924HG*	0.00	1.10	0.72	0.57	6.10640620425961E-203
201	10	*MMP9*	0.00	2.77	0.67	0.53	8.08397127732943E-193
202	10	*LAMC2*	0.00	2.72	0.97	0.74	0
203	10	*KRT6A*	0.00	2.63	0.89	0.67	0
204	10	*LAMA3*	0.00	2.51	0.8	0.65	2.88170788687901E-275
205	10	*LAMB3*	0.00	1.81	0.8	0.62	3.27852024209837E-276
206	10	*KRT17*	0.00	1.79	0.49	0.51	1.15843945877946E-40
207	10	*COL17A1*	0.00	1.77	0.68	0.59	5.38500051358062E-140
208	10	*INPP4B*	0.00	1.35	0.81	0.63	2.04825297095848E-212
209	10	*KRT14*	0.00	1.22	0.51	0.59	3.23324533571871E-21
210	10	*TMEM132D*	0.00	1.22	0.62	0.56	1.35736286299835E-92
211	10	*SEMA3C*	0.00	1.15	0.95	0.8	1.78100630981075E-230

212	10	*THBS1*	0.00	1.13	0.88	0.7	1.06459363129595E-135
213	10	*DSC2*	0.00	1.13	0.85	0.68	9.22506907450692E-173
214	10	*ITGB4*	0.00	1.12	0.49	0.45	3.83789725369348E-66
215	10	*TNS4*	0.00	1.09	0.42	0.52	1.58597324817715E-08
216	10	*NTN4*	0.00	1.09	0.69	0.56	8.74503754757718E-152
217	10	*ITGA6*	0.00	1.08	0.66	0.63	4.50495301171499E-66
218	10	*LINC00511*	0.00	1.08	0.84	0.57	1.39860819563529E-216
219	10	*FRMD6*	0.00	1.06	0.78	0.61	8.84377502264119E-144
220	10	*CHST11*	0.00	1.05	0.83	0.67	5.58462409190851E-165